





Reconciliation of weak pairwise spike–train correlations and highly coherent local field potentials across space

Johanna Senk ^{1,2,*†}, Espen Hagen ^{1,3,*†}, Sacha J. van Albada ^{1,4}, Markus Diesmann ^{1,5,6,7}

¹Institute for Advanced Simulation (IAS-6), Jülich Research Centre, Wilhelm-Johnen-Str., 52428 Jülich, Germany

²Sussex AI, School of Engineering and Informatics, University of Sussex, Chichester, Falmer, Brighton BN1 9QJ, United Kingdom

³Centre for Precision Psychiatry, Institute of Clinical Medicine, University of Oslo, and Division of Mental Health and Addiction, Oslo University Hospital, Ullevål Hospital, 0424 Oslo, Norway

⁴Institute of Zoology, University of Cologne, Zùlpicher Str., 50674 Cologne, Germany

⁵JARA-Institute Brain Structure-Function Relationships (INM-10), Jülich Research Centre, Wilhelm-Johnen-Str., 52428 Jülich Germany

⁶Department of Psychiatry, Psychotherapy and Psychosomatics, Medical Faculty, RWTH Aachen University, Pauwelsstr., 52074 Aachen, Germany

⁷Department of Physics, Faculty 1, RWTH Aachen University, Otto-Blumenthal-Str., 52074 Aachen, Germany

*Corresponding authors: Johanna Senk, Email: j.senk@fz-juelich.de; Espen Hagen, Email: espen.hagen@medisin.uio.no

†Johanna Senk and Espen Hagen contributed equally.

Multi-electrode arrays covering several square millimeters of neural tissue provide simultaneous access to population signals such as extracellular potentials and spiking activity of one hundred or more individual neurons. The interpretation of the recorded data calls for multiscale computational models with corresponding spatial dimensions and signal predictions. Multi-layer spiking neuron network models of local cortical circuits covering about 1 mm^2 have been developed, integrating experimentally obtained neuron-type-specific connectivity data and reproducing features of observed in-vivo spiking statistics. Local field potentials can be computed from the simulated spiking activity. We here extend a local network and local field potential model to an area of $4 \times 4\text{ mm}^2$, preserving the neuron density and introducing distance-dependent connection probabilities and conduction delays. We find that the upscaling procedure preserves the overall spiking statistics of the original model and reproduces asynchronous irregular spiking across populations and weak pairwise spike–train correlations in agreement with experimental recordings from sensory cortex. Also compatible with experimental observations, the correlation of local field potential signals is strong and decays over a distance of several hundred micrometers. Enhanced spatial coherence in the low-gamma band around 50 Hz may explain the recent report of an apparent band-pass filter effect in the spatial reach of the local field potential.

Key words: distance-dependent connectivity; extracellular signals; large-scale computational model; multi-layer cortical network; spiking neural network simulation.

Introduction

Cortical activity on the mesoscopic scale (*mesoscale*—spanning several millimeters to centimeters; Muller et al. 2018)—can be recorded with implanted multi-electrode arrays (Maynard et al. 1997; Buzsáki et al. 2012). The local field potential (LFP) is the low-frequency part ($\lesssim 500\text{ Hz}$) of the measured extracellular signal, primarily reflecting synaptic activations (Einevoll et al. 2013; Haines et al. 2024) across millions of local and distant neurons (Kajikawa and Schroeder 2011; Lindén et al. 2011; Łęski et al. 2013). Spike sorting (Quiroga 2007) extracts spikes of individual neurons from the high-frequency part ($\gtrsim 100\text{ Hz}$) of the signal. From Utah array recordings (10×10 electrodes on $4 \times 4\text{ mm}^2$, Blackrock Neurotech, <https://blackrockneurotech.com>) one may identify spiking activity of $\mathcal{O}(100)$ neurons (Riehle et al. 2013). Such recordings also expose propagating LFP activity associated with distance dependence of statistical measures like correlations and coherences (Destexhe et al. 1999; Smith and Kohn 2008; Wu et al. 2008; Dubey and Ray 2016), contrasting the low pairwise correlation in cortical spike trains characteristic of asynchronous brain states (e.g. Ecker et al. 2010).

Assuming a neuron density of $\mathcal{O}(10^5)$ neurons/ mm^2 across the human cortical surface (Herculano-Houzel 2009), a Utah array covers over a million neurons. Every neuron receives up to $\mathcal{O}(10^4)$ synapses from both nearby and distant neurons (Abeles 1991; Sherwood et al. 2020), forming local circuits specific to cortical layers and neuron types (Douglas et al. 1989; Thomson et al. 2002; Binzegger et al. 2004; Korcsak-Gorzo et al. 2024). Most local cortical connections onto postsynaptic neurons occur within $\lesssim 500\text{ }\mu\text{m}$ from presynaptic neurons (Voges et al. 2010), with connection probabilities decaying approximately exponentially with distance (Perin et al. 2011). Local intracortical connections are typically made by unmyelinated axons, leading to conduction delays governed by axonal propagation speeds of around 0.3 mm/ms (Hirsch and Gilbert 1991), which is in line with mesoscopic wave propagation speeds (Sato et al. 2012; Denker et al. 2018; Muller et al. 2018).

The relationship between cortical connectivity and experimentally recorded spikes and LFPs at the mesoscale remains poorly understood. Network models encompassing the relevant anatomical and physiological detail, spatial scales, and corresponding measurements can aid the interpretation of

Received: November 7, 2023. Revised: September 9, 2024. Accepted: September 23, 2024

© The Author(s) 2024. Published by Oxford University Press.

This is an Open Access article distributed under the terms of the Creative Commons Attribution Non-Commercial License (<https://creativecommons.org/licenses/by-nc/4.0/>), which permits non-commercial re-use, distribution, and reproduction in any medium, provided the original work is properly cited. For commercial re-use, please contact journals.permissions@oup.com

experimental observations. We advocate for full-scale models with realistic neuron and synapse counts: downscaled or diluted models may not reproduce first- and second-order statistics of full-scale networks (Albada et al. 2015). Hagen et al. (2016) demonstrate that biophysics-based predictions of LFP signals also require the full density of cells and connections to account for network correlations. The microcircuit model by Potjans and Diesmann (2014) is a full-density model of a 1 mm² patch of early sensory cortex with neuron-type- and layer-specific connection probabilities derived from anatomical and electrophysiological data. This model produces biologically plausible firing rates across four cortical layers with one excitatory and inhibitory population per layer, permits rigorous mathematical analysis, is freely available, and is actively used by the community in neuroscientific studies (e.g. Wagatsuma et al. 2011; Cain et al. 2016; Schwalger et al. 2017; Schmidt et al. 2018a) and as a benchmark model for neuromorphic computing (e.g. Albada et al. 2018; Kauth et al. 2023).

Here, we upscale a version of this microcircuit model (adapted to area V1 of macaque cortex by Schmidt et al. 2018a) to the cortical surface covered by Utah arrays, introducing distance-dependent connectivity and corresponding LFP measurements. We hypothesize that this upscaled model not only preserves original activity features but also elucidates mesoscale phenomena such as the spatial propagation of evoked neuronal activity (Bringuier et al. 1999; Muller et al. 2014) and strong distance-dependent correlations and coherences in the measured LFP (Destexhe et al. 1999; Katzner et al. 2009; Nauhaus et al. 2009; Jia et al. 2011; Kajikawa and Schroeder 2011; Srinath and Ray 2014; Dubey and Ray 2016), even for network states with weak pairwise spike-train correlations (e.g. Ecker et al. 2010; Dahmen et al. 2022).

Materials and methods

Point-neuron networks

The *reference model* (illustrated in Fig. 1A, parameters with superscript *r*) is extended to the larger *upscaled model* (illustrated in Fig. 1B, parameters with superscript *u*) by spatial structure. Tables 1 and 2 provide the full network descriptions. Each model represents a part of early sensory cortex at full neuron and synapse density. The eight neuron populations within each network are organized into four cortical layers, that is, layer 2/3 (L2/3), layer 4 (L4), layer 5 (L5) and layer 6 (L6). Each layer contains an excitatory (E) and an inhibitory (I) population of leaky integrate-and-fire (LIF) model neurons, whose sub-threshold membrane dynamics are governed by Equation (14).

The probabilities for two neurons to be connected are specific to the combination of source and target population and derived from a number of anatomical and electrophysiological studies (Potjans and Diesmann 2014). The reference model is further refined to area V1 of macaque cortex using the parameterization of the multi-area model proposed by Schmidt et al. (2018a,b). Postsynaptic currents have static, normally distributed amplitudes and decay exponentially Equations (15) and (16). All neurons receive stationary external input in the form of Poisson spike trains with a fixed rate; this input here also compensates for missing connections from other areas of the multi-area model. In addition, one population of thalamocortical (TC) neurons targeting E and I neurons in both L4 and L6 can provide further external input, for example, to emulate stimuli of the sensory pathway. We refer to the total set of populations as $X_{\text{total}} = X_E \cup X_I$, where $X_E = \{L2/3, L4, L5, L6\} \times \{E\} \cup \{TC\}$ is the subset of

excitatory populations and $X_I = \{L2/3, L4, L5, L6\} \times \{I\}$ is the subset of inhibitory populations, respectively. The connectivity is defined via projections from a presynaptic population $X \in X_{\text{total}}$ to a postsynaptic population $Y \in X_{\text{total}} \setminus \{TC\}$. Thus, we use the distinction between *connections* (i.e. atomic edges between individual network nodes) and *projections* (i.e. collections of connections) introduced by Senk et al. (2022).

Both network models are available as executable descriptions in the language consumed by the simulation code NEST (<http://www.nest-simulator.org>; Gewaltig and Diesmann 2007; Graber et al. 2024). Upon execution, the simulation engine instantiates a realization of the network model the main memory of the computer based on the statistical description of network connectivity. The model specifications are set up such that the same code is used for both the reference and the upscaled model, but with different parameters. The model code is publicly available on GitHub (<https://github.com/INM-6/mesocircuit-model>).

The following explains how the upscaled model is derived from the reference model, highlights the differences between the two, and provides a justification for choices of parameter values (Tables 3 and 4).

Neuron numbers and space

In the reference model, each population X is composed of N_X^r neurons. This model represents the cortical tissue below a surface area of $A^r = 1 \text{ mm}^2$ but neurons are not assigned spatial coordinates.

The upscaled model assigns spatial coordinates to neurons in two dimensions. Neuron positions are drawn randomly from a uniform distribution within a square domain of side length $L = 4 \text{ mm}$ with the origin (0, 0) at the center. The area covered by the model is therefore $A^u = L^2$. The neuron densities per square millimeter of the reference model are preserved, so the size of a population X in the upscaled model is

$$N_X^u = N_X^r \frac{A^u}{A^r}. \quad (1)$$

The reference model comprises 198,834 neurons and 388,515,188 synapses under 1 mm² of cortical surface area, while the upscaled model consists of 3,181,344 neurons and 7,661,094,874 synapses and covers an area of 4 × 4 mm², similar to the area covered by the Utah multi-electrode array.

Synaptic time constants and strengths

The reference model uses the same synaptic time constant τ_s^r for all projections. Synaptic strengths in this model are proportional to synaptic strength J with a projection-specific factor g_{YX}^r for projections from population X to population Y . The upscaled model uses different synaptic time constants for excitatory and inhibitory projections: $\tau_{s,E}^u$ and $\tau_{s,I}^u$, respectively. To preserve the total charge, i.e. the integral of a postsynaptic current due to a presynaptic spike, we compensate synaptic weights by adjusting the relative synaptic strengths:

$$g_{YX}^u = g_{YX}^r \cdot \begin{cases} \tau_s^r / \tau_{s,E}^u & \text{if } X \in X_E \\ \tau_s^r / \tau_{s,I}^u & \text{if } X \in X_I. \end{cases} \quad (2)$$

Note that the default factor for inhibitory projections is $g_{YX}^r = 11$ for $X \in X_I$ as in the model by Schmidt et al. (2018a) instead of 4 as in the original model by Potjans and Diesmann (2014). Inhibitory postsynaptic potential amplitudes tend to be larger

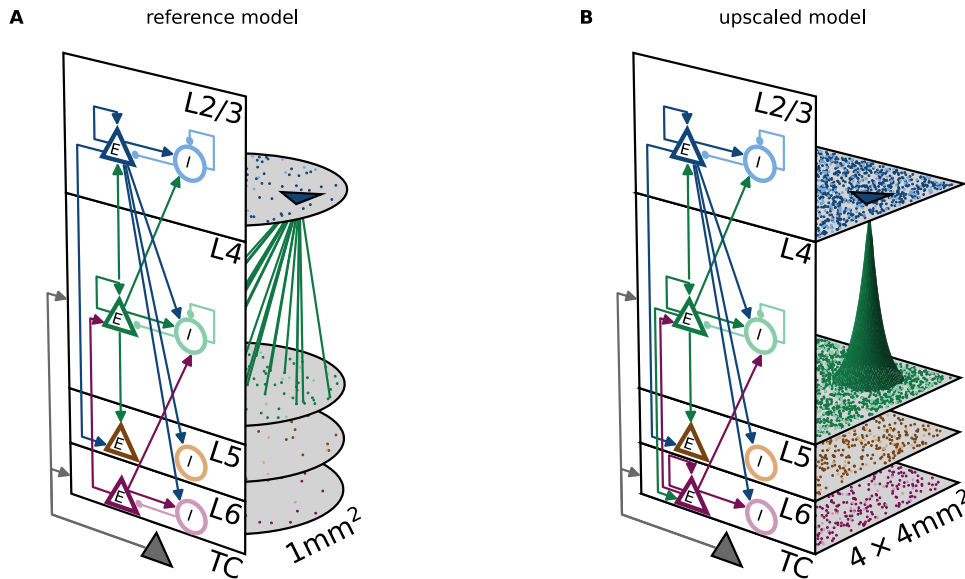


Fig. 1. Comparison of point-neuron network models. **A** Reference model (1mm² cortical microcircuit without spatial organization, adapted from the model introduced by Potjans and Diesmann 2014 to macaque V1 by Schmidt et al. 2018a). **B** Upscaled model (4 × 4 mm² in two-dimensional layers with spatial organization). Both models represent four cortical layers (L2/3, L4, L5, L6) with an excitatory (E) and an inhibitory (I) population each, and an external thalamic population (TC). The 2D network sketches illustrate by arrows the main population-specific projections (only projections with an average in-degree larger than 300 shown; for all in-degrees see Fig. 2B,E). The 3D representation exemplifies connections from L4E to a target neuron in L2/3E (no spatial dependence in reference model, exponential local connectivity profile in upscaled model). Layer thicknesses in the sketches are proportional to the neuron numbers per layer; cell bodies (dots) projected to bottom of layer to indicate that cortical depth within layer has no relevance for model.

than excitatory ones, but a factor of 11 is most likely overestimated (Avermann et al. 2012). However, here we follow the model of Schmidt et al. (2018a) to obtain a plausible dynamical state in the reference model.

In the upscaled model, the time constants of postsynaptic currents are $\tau_{s,E}^u = 2$ ms and $\tau_{s,I}^u = 8$ ms for excitatory and inhibitory projections, respectively, versus $\tau_s^r = 0.5$ ms used for all synapses in the reference model. This change between the reference and upscaled model accounts for the observed differences in decay time constants of AMPA and GABA_A synaptic conductances. The $\tau_{s,E}^u$ and $\tau_{s,I}^u$ values are inferred from synaptic conductance decay time constants used in the model by Markram et al. (2015), via model files available on the Neocortical Microcircuit Collaboration Portal (Ramaswamy et al. 2015). We ignored the short rise time constants. Synaptic NMDA currents with very long time constants are not accounted for. The adjustment of the synaptic strengths to preserve the total electric charge delivered by the postsynaptic currents in the reference model (Equation (2)) reduces the relative strength of inhibition to a factor of -2.75 compared to the factor of -11 in the reference model.

Connectivity

In the reference model, a neuron j in a source population X of size N_X^r connects at random to a neuron i in a target population Y of size N_Y^r with mean connection probability (Potjans and Diesmann 2014, Equation 1)

$$C_{YX}^r = 1 - \left(1 - \frac{1}{N_X^r N_Y^r}\right)^{S_{YX}^r}, \quad (3)$$

where S_{YX}^r denotes the total number of synapses between these populations. The connection routine randomly samples pairs of neurons with replacement and connects them until the total number of synapses S_{YX}^r is reached. Multiple connections (*multapses*) between neuron pairs are therefore allowed. Thus, C_{YX}^r

defines the probability that a pair of neurons is connected via one or more synapses. Here, we start with the mean in-degree K_{YX}^r , the number of incoming connections to a neuron $i \in Y$ from the source population X , such that the total number of synapses entering the connection routine is $S_{YX}^r = K_{YX}^r \cdot N_Y^r$. External Poisson input is provided to each population with in-degree $K_{X,ext}^r$.

In contrast to the uniform connectivity in the reference model, the upscaled model is characterized by a spatial network organization realized with distance-dependent projections. A source neuron $j \in X$ at location (x_j, y_j) connects to a target neuron $i \in Y$ at location (x_i, y_i) with a probability dependent on their spatial separation r_{ij} given in Equation (12). This expression for distance accounts for periodic boundary conditions (torus connectivity). The distance-dependent connection probability is shaped as a two-dimensional exponential with spatial width b_{YX} , up to a cutoff radius, as defined in Equation (13). We set the cutoff radius R_{YX} to where the probability of drawing a connection is below 1%. The spatial widths depend on the types (i.e. excitatory or inhibitory) of the pre- and postsynaptically connected cells. The connectivity in the upscaled model is derived as follows from the reference model:

- 1) Scale in-degrees of reference model to the extent of the upscaled model. Here, we assume that both models have the same underlying spatial profile, but the reference model only allows for the very local connections to be realized within the recurrent network. The in-degrees of the upscaled model are

$$K_{YX}^u = k^{u/r} \cdot K_{YX}^r \cdot k_{YX} \quad (4)$$

with the scaling factor

$$k^{u/r} = I(R)/I(Q) \quad (5)$$

accounting for the relative surface areas of the upscaled and reference models. $I(R)$ and $I(Q)$ are defined as the integrals in polar coordinates over the exponential profile without zero-distance connection probability,

$$I(A) := \int_0^A r \cdot e^{-\frac{r}{b_{YX}}} dr = b_{YX}^2 \cdot \left(1 - e^{-\frac{A}{b_{YX}}} \cdot \left(1 + \frac{A}{b_{YX}}\right)\right), \quad (6)$$

with radius $R = L/2$ for the upscaled model and $Q = 1/\sqrt{\pi}$ mm for the reference model, respectively. Note that this simple calculation does not account for the cutoff radius, but the deviation is marginal. The additional factor k_{YX} applied in this step is used to further scale selected in-degrees of specific pairs of pre- and postsynaptic projections.

- 2) Compute the zero-distance connection probability. For a uniform connectivity profile within a disc of the cutoff radius, $c_{ij}^{\text{uni}} = c_{YX}^{\text{uni}} \Theta(R_{YX} - r_{ij})$, and our exponential profile $c^u(r_{ij})$ defined in Equation (13) to cause the same average in-degree, we request the integral over both profiles to be the same (calculated in polar coordinates: $\int_0^\infty r \cdot c(r) dr$). The uniform connection probability relies on the number of potential source neurons, which is proportional to the area of the disc divided by the total extent of the modeled cortical sheet:

$$c_{YX}^{\text{uni}} = \frac{K_{YX}^u}{N_X^u \cdot \pi R_{YX}^2 / L^2}. \quad (7)$$

The zero-distance connection probability is derived as follows:

$$\begin{aligned} \int_0^\infty r \cdot c_{YX}^{\text{uni}} dr &= \int_0^\infty r \cdot c_{YX}^u e^{-\frac{r}{b_{YX}}} dr \\ \Leftrightarrow c_{YX}^u &= \frac{0.5 \cdot R_{YX}^2 \cdot c_{YX}^{\text{uni}}}{I(R_{YX})} = \frac{K_{YX}^u \cdot L^2}{2\pi \cdot N_X^u \cdot I(R_{YX})}, \end{aligned} \quad (8)$$

using the definition of $I(A)$ from Equation (6).

- 3) Adjust the external in-degrees to preserve the mean input. Since the upscaled model has a different number of recurrent connections compared to the reference model, the external Poisson input of rate v_{ext} needs to be adapted to compensate:

$$K_{Y,\text{ext}}^u = \left(K_{Y,\text{ext}}^r + \sum_X \frac{v_X}{v_{\text{ext}}} \frac{g_{YX}^r}{g_{\text{ext}}^r} (K_{YX}^r - K_{YX}^u) \right) \cdot k_{\text{ext},Y} \cdot k_{\text{ext}} \quad (9)$$

This modification of external in-degrees in the upscaled network only preserves the mean of the spiking input (which is proportional to both in-degrees and weights), but not its variance (which is proportional to in-degrees and to weights squared); see, for example, Brunel and Hakim (1999) and Albada et al. (2015) for details. Analogous to the factor k_{YX} for scaling recurrent in-degrees, we here introduce the factor $k_{\text{ext},Y}$, which allows for further scaling of selected external in-degrees. In addition, the population-independent factor k_{ext} equally scales all external in-degrees.

Synapses are drawn according to a pairwise Bernoulli rule with probabilities given by the spatial profile, and each pair of neurons is considered only once. Thus, multapses are not allowed and the total number of synapses is not fixed in the upscaled model, in contrast to the reference model.

The decay constants b_{YX} of the exponential profile (Table 4) used in the upscaled model are taken from Reimann et al. (2017, Figure S2); the study provides mean space constants of exponential fits to the distance-dependent connection probabilities for the four projection types between excitatory and inhibitory neurons based on morphologically classified cell types in an anatomical reconstruction and simulation of rat somatosensory cortex (Markram et al. 2015). Other experimental data also indicate exponentially or Gaussian decaying connection probabilities with distance for both excitatory and inhibitory local connections with space constants of similar magnitude; see the review by Boucsein et al. (2011) and Table 5 for a summary. Such profiles are explained by axo-dendritic overlap of the neuronal morphologies (Amirikian 2005; Brown and Hestrin 2009; Hill et al. 2012). In our model, the excitatory-to-excitatory projections have the largest decay constant. Broader excitation than inhibition is in line with the experimental data since excitatory neurons, in particular pyramidal neurons, develop axons with larger horizontal reach compared to most inhibitory interneuron types (Budd and Kisvárdy 2001; Binzegger et al. 2004; Buzás et al. 2006; Binzegger et al. 2007; Stepanyants et al. 2007, 2009; Ohana et al. 2012). Certain interneuron types may, however, have elaborate axons that span and form synapses across different layers within the cortical column (see, for example, Markram et al. 2015, Figure 2). Others may also form longer-range lateral connections (McDonald and Burkhalter 1993). Connections in the upscaled model are mostly local since all decay constants are less than 0.25 mm. This locality is reflected by similar in-degrees in both models (Fig. 2).

Synaptic transmission delays

In the reference model, connection delays are normally distributed according to Equation (18) with a standard deviation of half the mean delay. The excitatory mean delay is twice as long as the inhibitory one. If a sampled delay is smaller than the simulation time step h , it gets redrawn, resulting in a truncated normal distribution.

The upscaled model uses a linear distance dependence given by Equation (19) with a constant delay offset $d_0 = 0.5$ ms and a conduction speed $v = 0.3$ mm/ms. The delay offset mimics transmission processes locally at the synapse, and the conduction speed is in the range of speeds reported for action potential propagation along unmyelinated nerve fibers in cortex (for a comparison with experimental estimates see Table 5). Conduction speeds can be measured, for example, in brain slices using electrical stimulation combined with electrophysiological recordings. Some of these values are likely underestimated because the separation of conduction speed from both the synaptic delay and spike initiation time is difficult (Hirsch and Gilbert 1991). The bath temperatures are provided if specified by the study because the conduction speed and the timing of synaptic processing depend strongly on environmental temperature (Katz and Miledi 1965; Berg-Johnsen and Langmoen 1992; Sabatini and Regehr 1996; Hardingham and Larkman 1998). We are here primarily interested in physiologically relevant body temperatures.

We compare the mean delays of the reference model \bar{d}_X^r with effective mean delays of the upscaled model \bar{d}_{YX}^u obtained by averaging delays on a disc of 1 mm^2 (with radius $Q = 1/\sqrt{\pi}$ mm), thus equaling the extent of the reference model. Accounting for all distances between random points on the disc and connectivity governed by the exponentially shaped profile with the spatial width b_{YX} , the effective delay in polar coordinates for a disc of

radius Q is

$$\bar{d}_{YX}^u(Q) = \frac{1}{\pi^2 Q^4} \int_0^Q \int_0^{2\pi} \int_0^Q \int_0^{2\pi} \left(d_0 + \frac{r_{21}}{v}\right) \times \frac{1}{c_{\text{norm}}} e^{-\frac{r_{21}}{b_{YX}}} r_1 r_2 d\varphi_1 dr_1 d\varphi_2 dr_2 \quad (10)$$

with $r_{21} = r_1^2 + r_2^2 - 2r_1 r_2 \cos(\varphi_1 - \varphi_2)$. The spatial profile is here normalized to unity for the integral over the disc by the factor c_{norm} and we ignore the Heaviside function because we only consider $Q < R_{YX}$. The expression simplifies (Sheng 1985, Theorem 2.4) to

$$\bar{d}_{YX}^u(Q) = \frac{\int_0^{2Q} (d_0 + \frac{r}{v}) \exp(-\frac{r}{b_{YX}}) r \left(4 \arctan\left(\sqrt{\frac{2Q-r}{2Q+r}}\right) - \sin\left(4 \arctan\left(\sqrt{\frac{2Q-r}{2Q+r}}\right)\right)\right) dr}{\int_0^{2Q} \exp(-\frac{r}{b_{YX}}) r \left(4 \arctan\left(\sqrt{\frac{2Q-r}{2Q+r}}\right) - \sin\left(4 \arctan\left(\sqrt{\frac{2Q-r}{2Q+r}}\right)\right)\right) dr}, \quad (11)$$

which we evaluate numerically. Although delay offset and conduction speed have the same parameter values for excitatory and inhibitory projections in the upscaled model, the effective delays (Equation (11)) within a given surface area differ due to the different space constants of the connectivity. The computed mean

effective delays are

$$\begin{pmatrix} \bar{d}_{EE}^u & \bar{d}_{EI}^u \\ \bar{d}_{IE}^u & \bar{d}_{II}^u \end{pmatrix} = \begin{pmatrix} 1.513 & 1.319 \\ 1.185 & 1.164 \end{pmatrix} \text{ ms},$$

which are similar to the delays in the reference model, cf. Table 4. A shorter inhibitory delay in a network model without distance dependence like the reference model appears justified by a narrower inhibitory connectivity of the corresponding model with spatial structure.

Thalamic input

The thalamocortical neuron population of the reference model is set up as a spatially organized layer of the upscaled model in the same way as the cortical populations. Positioning thalamic neurons also uniformly within area A^u facilitates the connectivity management to the cortical populations. An analogy to the early visual pathway would be that the distance L in both thalamus and cortex corresponds to the same extent of the visual field. For the sake of this study, we only activate thalamic neurons within a disc of radius $R_{\text{pulse}}^{\text{TC}}$ surrounding the center such that they emit spikes

Table 1. Description of reference and upscaled network models following the guidelines of Nordlie et al. (2009).

A: Model summary	
Structure	Multi-layer excitatory-inhibitory (E-I) network
Populations	8 cortical populations in 4 layers (L2/3, L4, L5, L6) and 1 thalamic population (TC): $X_{\text{total}} = X_E \cup X_I$, $X_E = \{L2/3, L4, L5, L6\} \times \{E\} \cup \{TC\}$ and $X_I = \{L2/3, L4, L5, L6\} \times \{I\}$
Input	Cortex: independent fixed-rate Poisson spike trains to all neurons (population-specific in-degree)
Measurements	Spikes, LFP, CSD, MUA
Neuron model	Cortex: leaky integrate-and-fire (LIF); Thalamus: point process
Synapse model	Exponentially shaped postsynaptic currents with normally distributed static weights
<i>Reference model</i>	
Topology	None (no spatial information)
Delays	Normally distributed delays
Connectivity	Random, fixed total number with multapses (autapses prohibited)
<i>Upscaled model</i>	
Topology	Random neuron positions on square domain of size $L \times L$; periodic boundary conditions
Delays	Distance-dependent delays
Connectivity	Random, distance-dependent connection probability, population-specific, number of synapses not fixed in advance (autapses and multapses prohibited)
B: Network models	
Connectivity	In-degrees K_{YX} from population X to population Y with $X \in X_{\text{total}}$ and $Y \in X_{\text{total}} \setminus \{TC\}$
<i>Reference model</i>	
Random, fixed total number with multapses (autapses prohibited), see Senk et al. (2022) for a definition. Fixed number of synapses $S_{YX}^T = K_{YX}^T \cdot N_Y^T$ between populations X and Y with N_Y^T being the size of the target population.	
<i>Upscaled model</i>	
<ul style="list-style-type: none"> Presynaptic neuron $j \in X$ at location (x_j, y_j) and postsynaptic neuron $i \in Y$ at (x_i, y_i) Neuron inter-distance (periodic boundary conditions): 	
$r_{ij} = \sqrt{\Delta x_{ij}^2 + \Delta y_{ij}^2}$	
with $\Delta x_{ij} = x_i - x_j $ if $ x_i - x_j \leq L/2$, otherwise $\Delta x_{ij} = L - x_i - x_j $ (same for Δy_{ij})	
<ul style="list-style-type: none"> Exponentially shaped connection probability with spatial width b_{YX}, maximal distance $R_{YX} = 5 \cdot b_{YX}$, and zero-distance connection probability c_{YX}^u (see Equation (8)): 	
$c^u(r_{ij}) = c_{YX}^u e^{-r_{ij}/b_{YX}} \Theta(R_{YX} - r_{ij})$	
Heaviside function $\Theta(t) = 1$ for $t \geq 0$, and 0 otherwise.	
<ul style="list-style-type: none"> Autapses and multapses are prohibited 	

Table 2. Description of reference and upscaled network model (continuation of Table 1).

C: Neuron models	
Cortex	Leaky integrate-and-fire neuron (LIF) <ul style="list-style-type: none"> Dynamics of membrane potential $V_i(t)$ for neuron i: $\tau_m \dot{V}_i = -V_i + R_m I_i(t) \quad \text{if } \forall s: t \notin (t_s^i, t_s^i + \tau_{\text{ref}}] \quad \text{with } \tau_m = R_m C_m \quad (14)$ Spike emission at times $t_s^i \in \mathcal{S}_i = \{t_0^i, t_1^i, t_2^i, \dots\}$ with $V_i(t_s^i) \geq V_\theta$ Subthreshold dynamics: $\text{Reset + refractoriness: } V_i(t) = V_{\text{reset}} \quad \text{if } t \in (t_s^i, t_s^i + \tau_{\text{ref}}], t_s^i \in \mathcal{S}_i$ Exact integration with temporal resolution h (Rotter and Diesmann 1999) Random, uniform distribution of membrane potentials at $t = 0$
Thalamus	Spontaneous activity: no thalamic input ($v_{\text{TC}} = 0$)
<i>Upscaled model</i>	
Thalamus	Thalamic pulses: coherent activation of all thalamic neurons inside a circle with radius $R_{\text{TC}}^{\text{pulse}}$ centered around $(0, 0)$ at fixed time intervals Δt_{TC}
D: Synapse models	
Postsynaptic currents	<ul style="list-style-type: none"> Instantaneous onset, exponentially decaying postsynaptic currents Input current of neuron i from presynaptic neuron j: $I_i(t) = \sum_j J_{ij} \sum_s e^{-(t-t_s^j-d_{ij})/\tau_s} \Theta(t - t_s^j - d_{ij}) \quad (15)$
Weights	<ul style="list-style-type: none"> Normal distribution with static weights, truncated to preserve sign: $J_{ij} \sim \mathcal{N}\{\mu = g_{\text{YX}} \cdot J, \sigma^2 = \sigma_{\text{f,YX}}^2\} \quad (16)$ Probability density of normal distribution: $f(x \mu, \sigma^2) = \frac{1}{\sqrt{2\pi\sigma^2}} e^{-\frac{(x-\mu)^2}{2\sigma^2}} \quad (17)$
<i>Reference model</i>	
Delays	Normal distribution, truncated at h : $d_{ij} \sim \mathcal{N}\left\{\mu = \bar{d}_{\text{X}}, \sigma^2 = (\sigma_{\text{d,X}}^t)^2\right\} \quad (18)$
<i>Upscaled model</i>	
Delays	Linear distance dependence with delay offset d_0 and conduction speed v : $d(r_{ij}) = d_0 + \frac{r_{ij}}{v} \quad (19)$

in a synchronous and regular fashion (thalamic pulses) with time intervals Δt_{TC} , starting at time $t_{\text{TC,start}}$.

Forward modeling of extracellular potentials

In the present study, we use a well established scheme to compute extracellular potentials from neuronal activity. The method relies on multicompartment neuron modeling to compute transmembrane currents (see, for example, De Schutter et al. 2009) and volume conduction theory (Nunez and Srinivasan 2006; Einevoll et al. 2013; Halnes et al. 2024), which relates current sources and electric potentials in space. Assuming a volume conductor model that is linear (frequency-independent), homogeneous (the same in all locations), isotropic (the same in all directions), and ohmic (currents depend linearly on the electric field \mathbf{E}), as represented by the scalar electric conductivity σ_e , the electric potential in location $\mathbf{r} \equiv (x, y, z)$ of a time-varying point current with magnitude $I(t)$ in location \mathbf{r}' is given by

$$\phi(\mathbf{r}, t) = \frac{I(t)}{4\pi\sigma_e|\mathbf{r} - \mathbf{r}'|}. \quad (20)$$

The potential is assumed to be measured relative to an ideal reference at infinite distance from the source. Consider a set of transmembrane currents of n_{comp} individual cylindrical compartments indexed by n in an N -sized population of cells indexed by j with time-varying magnitude $I_{jn}^m(t)$ embedded in a volume

conductor representing the surrounding neural tissue. The extracellular electric potential is then calculated as

$$\phi(\mathbf{r}, t) = \sum_{j=1}^N \sum_{n=1}^{n_{\text{comp}}} \frac{I_{jn}^m(t)}{4\pi\sigma_e} \int \frac{1}{|\mathbf{r} - \mathbf{r}_{jn}|} d\mathbf{r}_{jn}. \quad (21)$$

The integral term reflects the use of the *line-source* approximation (Holt and Koch 1999) which amounts to assuming a homogeneous transmembrane current density per unit length and integrating Equation (20) along the center axis of each cylindrical compartment. The thick soma compartments (with $n = 1$) with magnitude $I_j^{\text{m.soma}}(t)$, however, are approximated as spherical current sources, which amounts to combining Equations (20) and (21) as (Lindén et al. 2014)

$$\begin{aligned} \phi(\mathbf{r}, t) &= \sum_{j=1}^N \frac{1}{4\pi\sigma_e} \left(\frac{I_j^{\text{m.soma}}(t)}{|\mathbf{r} - \mathbf{r}_j^{\text{soma}}|} + \sum_{n=2}^{n_{\text{comp}}} \int \frac{I_{jn}^m(t)}{|\mathbf{r} - \mathbf{r}_{jn}|} d\mathbf{r}_{jn} \right) \\ &= \sum_{j=1}^N \frac{1}{4\pi\sigma_e} \left(\frac{I_j^{\text{m.soma}}(t)}{|\mathbf{r} - \mathbf{r}_j^{\text{soma}}|} + \sum_{n=2}^{n_{\text{comp}}} \frac{I_{jn}^m(t)}{\Delta S_{jn}} \ln \left| \frac{\sqrt{h_{jn}^2 + r_{\perp jn}^2} - h_{jn}}{\sqrt{l_{jn}^2 + r_{\perp jn}^2} - l_{jn}} \right| \right). \end{aligned} \quad (22)$$

Table 3. Simulation, preprocessing, and global network parameters.

A: Global simulation parameters		
Symbol	Value	Description
$T_{\text{model},1}$	900,000 ms	Model time of spiking network simulation for comparison between reference and upscaled models
$T_{\text{model},2}$	10,000 ms	Model time of spiking network simulation for evoked activity
$T_{\text{model},3}$	5,000 ms	Model time of LFP simulation
h	0.1 ms	Temporal resolution
T_{pre}	1,000 ms	Model time of startup transient (presimulation time)
B: Preprocessing		
Symbol	Value	Description
Δt	0.5 ms	Temporal bin size
Δl	0.1 mm	Spatial bin size
C: Global network parameters		
Connection parameters and external input		
Symbol	Value	Description
J	87.81 pA	Reference synaptic strength. All synapse weights are measured in units of J .
$\sigma_{J,YX}$	$0.1 \cdot g_{YX} \cdot J$	Standard deviation of weight distribution
ν_{ext}	8 s^{-1}	Rate of external input with Poisson inter-spike interval statistics
LIF neuron model		
Symbol	Value	Description
C_m	250 pF	Membrane capacitance
τ_m	10 ms	Membrane time constant
E_L	−65 mV	Resistive leak reversal potential
V_θ	−50 mV	Spike detection threshold
V_{reset}	−65 mV	Spike reset potential
τ_{ref}	2 ms	Absolute refractory period after spikes

Here, the length of compartment n of cell j is denoted by Δs_{jn} , the perpendicular distance from the electrode point contact to the axis of the line compartment by $r_{\perp jn}$, and the longitudinal distance measured from the start of the compartment by h_{jn} . The distance $l_{jn} = \Delta s_{jn} + h_{jn}$ is measured longitudinally from the end of the compartment. As the above denominators can be arbitrarily small and cause singularities in the computed extracellular potential, we set the minimum separation $|\mathbf{r} - \mathbf{r}_j^{\text{soma}}|$ or $r_{\perp jn}$ equal to the radius of the corresponding compartment.

The above equations assume point electrode contacts, while real electrode contacts have finite extents. We employ the *disc-electrode approximation* (Camuñas Mesa and Quiroga 2013; Lindén et al. 2014; Ness et al. 2015)

$$\phi_{\text{disc}}(\mathbf{u}, t) = \frac{1}{A_S} \iint_S \phi(\mathbf{u}, t) d^2r \approx \frac{1}{m} \sum_{h=1}^m \phi(\mathbf{u}_h, t) \quad (23)$$

to approximate the averaged potential across the uninsulated contact surface (Robinson 1968; Nelson et al. 2008; Nelson and Pouget 2010; Ness et al. 2015). We average the potential (Equation (22)) in $m = 20$ randomized locations \mathbf{u}_h on each circular and flat contact surface S with surface area A_S and radius $5 \mu\text{m}$. The surface normal vector on the disc representing each contact is the unit vector along the vertical z -axis. All forward-model calculations are performed with the simulation tool LFPy (<https://lfpypy.readthedocs.io>, Lindén et al. 2014; Hagen et al. 2018), which uses the NEURON simulation software (<https://neuron.yale.edu>,

Carnevale and Hines 2006; Hines et al. 2009) to calculate trans-membrane currents.

The hybrid scheme for modeling extracellular signals

Our study calculates extracellular potentials from point-neuron network models using a modified version of the hybrid modeling scheme by Hagen et al. (2016). The scheme combines the forward modeling of extracellular potentials (i.e. LFPs) on the basis of spatially reconstructed neuron morphologies with recurrent network activity simulated using point-neuron networks. Point-neuron models alone cannot generate an extracellular potential, as the sum of all its in- and outgoing currents is zero. The validity of the hybrid scheme was recently revisited by Hagen et al. (2022). We refer to the Methods section of Hagen et al. (2016) for an in-depth technical description of the implementation for randomly connected point-neuron network models. Here, we only summarize the scheme's main steps and list the changes incorporated for networks with distance-dependent connectivity and periodic boundary conditions. As in Hagen et al. (2016), we assume that cortical network dynamics are well captured by the point-neuron network, and apply the hybrid scheme as follows:

- Spike trains of individual point neurons are mapped to synapse activation times on corresponding postsynaptic multicompartments neurons while overall connection parameters are preserved, that is, the distribution of delays, the mean postsynaptic currents, the mean number of incoming connections onto individual cells (in-degree), and the

Table 4. Additional network parameters for the reference and the upscaled models. Population sizes and in-degrees are given in Fig. 2.**D: Model-specific network parameters of the reference model****Connection parameters**

Symbol	Value	Description
g_{YX}^r	1	Relative synaptic strengths:
	2	$X \in X_E$, except for:
	–11	$(X, Y) = (L4E, L2/3E)$
τ_s^r	0.5 ms	$X \in X_I$
\bar{d}_E^r	1.5 ms	Postsynaptic current time constant
\bar{d}_I^r	0.75 ms	Mean excitatory delay
$\sigma_{d,X}^r$	$0.5 \cdot \bar{d}_X^r$	Mean inhibitory delay
		Standard deviation of delay distribution

E: Model-specific network parameters of the upscaled model**Connection parameters**

Symbol	Value	Description
g_{YX}^u	0.25	Derived relative synaptic strengths:
	0.5	$X \in X_E$, except for:
	–0.6875	$(X, Y) = (L4E, L2/3E)$
$\tau_{s,E}^u$	2 ms	$X \in X_I$
$\tau_{s,I}^u$	8 ms	Excitatory postsynaptic current time constant
d_0	0.5 ms	Inhibitory postsynaptic current time constant
v	0.3 mm/ms	Delay offset
$\begin{pmatrix} b_{EE} & b_{EI} \\ b_{IE} & b_{II} \end{pmatrix}$	$\begin{pmatrix} 0.232 & 0.161 \\ 0.125 & 0.120 \end{pmatrix}$ mm	Conduction speed
		Spatial widths of exponential connectivity profile

In-degree modifications

Symbol	Value	Description
k_{YX}	1	Scaling factor for in-degrees of recurrent connections
	1.8	$\{X, Y\} \in X_{\text{total}}$, except for:
	0.75	$(X, Y) = (L4I, L4I)$
	0.9	$(X, Y) = (L5E, L5I)$
	0.75	$(X, Y) = (L6I, L6I)$
	0.75	$(X, Y) = (L6E, L6I)$
$k_{\text{ext},Y}$	1	$(X, Y) = (L6I, L6E)$
	1.1	Scaling factor for external in-degrees to population Y
	1.08	$Y \in X_{\text{total}} \setminus \{\text{TC}\}$, except for:
k_{ext}	1.04	$Y = L2/3E$
		$Y = L4E$
		Global scaling factor for all external in-degrees

Thalamus

Symbol	Value	Description
$R_{\text{TC}}^{\text{pulse}}$	0.4 mm	TC neuron activation radius of disc around (0, 0), all TC neurons in the disc are active during pulses
σ_{TC}	0.1 mm	Spatial width of TC neuron connections
$t_{\text{TC,start}}$	1,000 ms	Start time for thalamic input
Δt_{TC}	100 ms	Interval between thalamic pulses

cell-type and layer specificity of connections is preserved, as in Hagen et al. (2016).

- The multicompartment neurons are mutually unconnected, and synaptic activations result in transmembrane currents that contribute to the total LFP.
- Activity in multicompartment neuron models (and the corresponding LFP) does not interact with other multicompartment neurons or the activity in the point-neuron network model, that is, there are no synaptic or ephaptic interactions.
- Each population $Y \in X_{\text{total}} \setminus \{\text{TC}\}$ of neurons in the point-neuron network may map to a number of cell types y in the

multicompartment representation. An overview of the choice of morphologies representing each cell type (M_y), segment count per morphology (n_{comp}), occurrence (F_y), relative occurrence (F_{yY}) per population, and final cell count is given in Table 6. The corresponding morphologies and layer boundaries are shown in Fig. 7.

The first version of the hybrid scheme implemented in hybridLFPy (<https://INM-6.github.com/hybridLFPy>) is developed for random networks such as the layered cortical microcircuit model of Potjans and Diesmann (2014). In contrast to this

Table 5. Comparison of selected model parameters with experimental data. The notation \pm refers to mean \pm standard deviation.

Connection parameters		
Delay offset (upscaled model: $d_0 = 0.5$ ms)		
Value (ms)	Data acquisition	Reference
0.5 – 1	rat visual cortex ($31 \pm 0.5^\circ\text{C}$)	Murakoshi et al. (1993)
0.6 – 0.8	cat visual cortex ($34 - 35^\circ\text{C}$)	Hirsch and Gilbert (1991)
0.6	cat motor cortex (35°C)	Kang et al. (1994)
Conduction speed (upscaled model: $v = 0.3$ mm/ms)		
Value (mm/ms)	Data acquisition	Reference
0.2 – 0.35	guinea pig hippocampus	Andersen et al. (1978)
$1/3.5 \approx 0.29$	cat visual cortex ($34 - 35^\circ\text{C}$)	Hirsch and Gilbert (1991)
0.3	rat hippocampus (35°C)	Berg-Johnsen and Langmoen (1992)
0.15 – 0.55	rat visual cortex ($31 \pm 0.5^\circ\text{C}$)	Murakoshi et al. (1993)
0.28 – 0.48 (0.37 ± 0.37)	cat motor cortex (35°C)	Kang et al. (1994)
0.28 ± 0.19	rat visual cortex (34°C)	Lohmann and Rörig (1994)
0.06 – 0.2	rat somatosensory cortex ($34 - 35^\circ\text{C}$)	Salin and Prince (1996)
0.508	rat somatosensory cortex ($32 - 35^\circ\text{C}$), back-propagating action potentials in dendrites	Larkum et al. (2001)
Distance-dependent connection probability (upscaled model, exponential decay: $\begin{pmatrix} b_{EE} & b_{EI} \\ b_{IE} & b_{II} \end{pmatrix} = \begin{pmatrix} 0.232 & 0.161 \\ 0.125 & 0.120 \end{pmatrix}$ mm)		
Value (mm)	Data acquisition	Reference
Gaussian fit: 0.2967 – 0.6208	pyramidal cells in layers 2 and 3 of rat visual cortex	Hellwig (2000)
exponential fit: 0.0488 – 0.05198	clutch cells in layer 4 of cat visual cortex	Budd and Kisvárdy (2001)
exponential fit: 0.124 – 0.183	parvalbumin-positive cells connected to pyramidal cells in multiple layers of mouse neocortex	Packer and Yuste (2011)
most connections: < 0.3	pyramidal cells in layer 5 of rat somatosensory cortex	Perin et al. (2011)
Gaussian fit: 0.085 – 0.114	pyramidal cells and (non-)fast-spiking inhibitory cells in deep layer 2/3 and layer 4 of mouse auditory cortex	Levy and Reyes (2012)
exponential fit: 0.141 – 0.352	excitatory input to pyramidal neurons in layer 5B of rat somatosensory cortex	Schnepel et al. (2015)
most connections: < 0.25	pyramidal cells and different interneurons in layers 1, 2/3, and 5 of mouse visual cortex	Jiang et al. (2015)
exponential fit: 0.125 – 0.232	morphologically classified cell types in an anatomical reconstruction and simulation of rat somatosensory cortex (Markram et al. 2015)	Reimann et al. (2017)

model that contains no spatial information, the upscaled model (Section [Point-neuron networks](#)) assigns spatial coordinates to the neurons within each layer but still ignore information about cortical depth, and draw connections between neurons with probabilities depending on lateral distance. Modifications to the hybrid scheme accounting for spatially organized networks include the following:

- Multicompartment neuron models inherit their lateral locations from their point-neuron counterparts. Population-dependent somatic depths are defined as in [Hagen et al. \(2016\)](#).
- The spiking activity from all neurons in the point-neuron network is recorded and indexed by the corresponding neuron ID.
- Presynaptic neuron IDs are drawn randomly for each multicompartment neuron governed by the same distance-dependent probability as is used when constructing the point-neuron network. The connectivity is thus statistically reproduced. The same distance-dependent delay rule is also implemented in the hybrid scheme, and can be set separately for each pair of populations.

- The extracellular potential is computed at 100 contact sites arranged on a square regular grid with each contact separated by $400 \mu\text{m}$, similar to the layout of the Blackrock ‘Utah’ multi-electrode array, and at a depth corresponding to the center of layer 2/3 (L2/3). The signal predictions account for periodic boundary conditions as described next.

Modifications of the forward model to account for periodic boundary conditions

As the upscaling procedure of the 1 mm^2 reference point-neuron network model incorporates periodic boundary conditions, we modify the calculations of extracellular potentials accordingly. The premise for this modification is that transmembrane currents of a neuron positioned near the lateral network layer boundary should contribute to the extracellular potential as sources across the boundary. This is analogous to input from network connections across the boundaries resulting from the distance-dependent connectivity rule. Here, this modification is implemented by accounting for additional “imaginary” transmembrane current sources. Equation (23) computes the extracellular

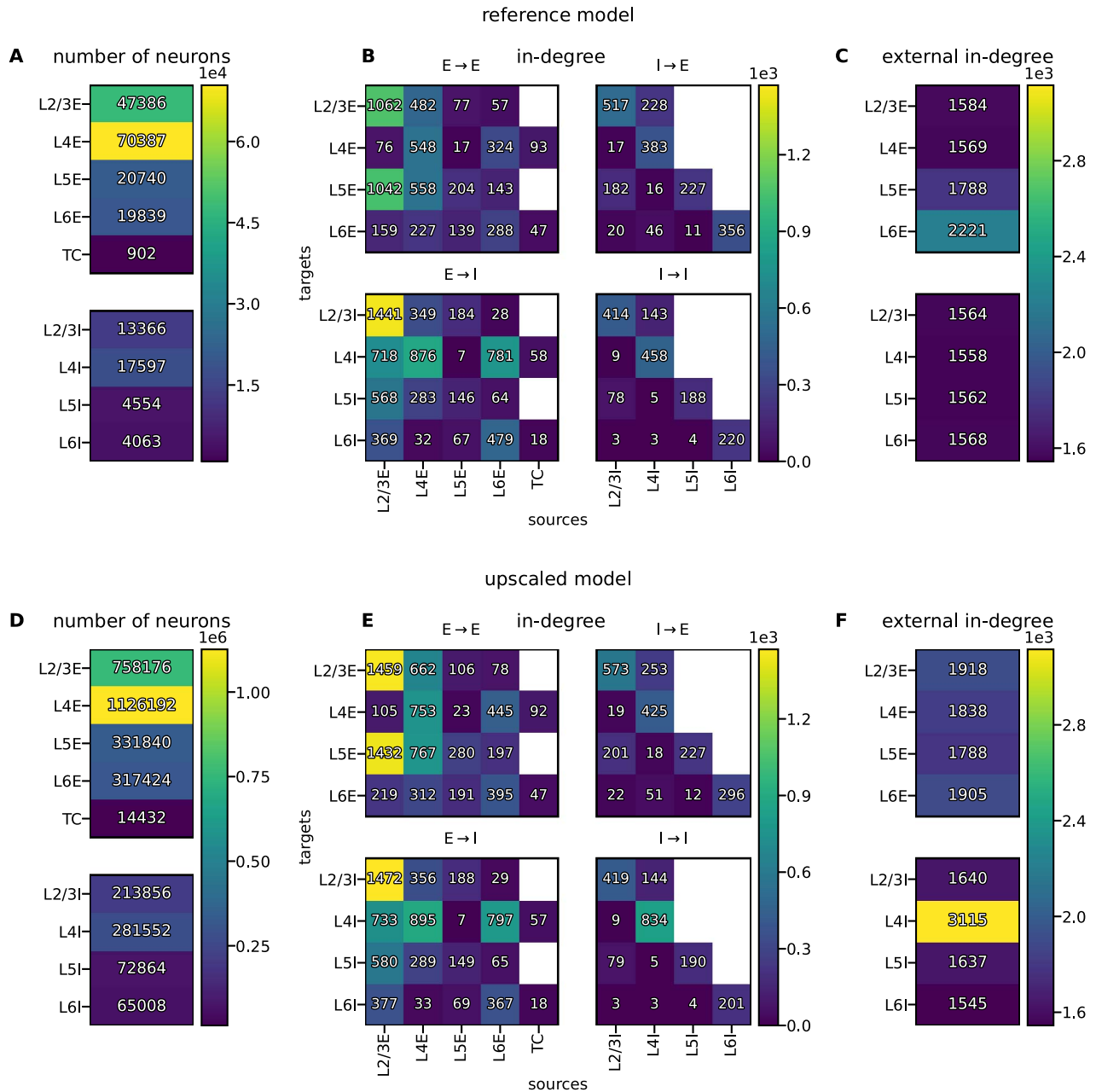


Fig. 2. Neuron numbers, average in-degrees of recurrent projections, and external in-degrees. **A–C** Reference model. **D–F** Upscaled model. Color codes are identical for in-degrees but not for neuron numbers; values of zero are colorless.

potential at location \mathbf{r} by iterating over all true current sources, i.e. each neuron located on the $L \times L$ domain with side length L . We assume that the sheet is surrounded by eight identical domains such that the potential at location \mathbf{r} in the center sheet receives contributions from within an extended area of size $3L \times 3L$. In other words, for each current source we sum up contributions from across both the true and all eight imaginary sheets, taking into account their distances to \mathbf{r} on the notionally extended cortical sheet.

Model signal predictions

As simulation output, we consider the spiking activity of the point-neuron networks (Section [Point-neuron networks](#)), and corresponding multi-unit activity (MUA), LFP (Section [Forward modeling of extracellular potentials](#)), and current-source

density (CSD) estimates. We use simulated output data only after an initial period T_{pre} of model presimulation time to avoid startup transients, and compute all measures for the whole time interval of the subsequent simulation (model times $T_{\text{model},1}$, $T_{\text{model},2}$, and $T_{\text{model},3}$).

Temporal binning of spike trains

Spike times t_i^s of the point-neuron networks simulated using temporal resolution h are assigned to bins with width Δt . Temporally binned spike trains are used to compute pairwise spike-train correlations and population-rate power spectral densities (PSDs), and to illustrate population-averaged rate histograms. The bin width Δt is an integer multiple of the simulation resolution h . The simulation duration T_{model} is an integer multiple of the bin width such that the number of bins is $K = T/\Delta t$. Time

Table 6. Summary of cell-type specific population and morphology parameters for extracellular signal predictions via the hybrid scheme.

Layer	Population Y	Pop. size N_Y	Cell type y	Morphology M_y	Segments n_{comp}	Occurrence $F_y(\%)$	Rel. occurrence $F_{YY}(\%)$	Cell count N_y
2/3	L2/3E	758,176	p23	p23	689	23.9	100.0	758,176
			b23	i23	324	2.9	42.5	90,816
			nb23	i23	324	3.9	57.5	123,040
4	L4E	1,126,192	p4	p4	603	11.9	33.3	375,397
			ss4(L2/3)	ss4	339	11.9	33.3	375,397
			ss4(L4)	ss4	339	11.9	33.3	375,397
	L4I	281,552	b4	i4	230	7.0	78.3	220,345
			nb4	i4	230	1.9	21.7	61,207
5	L5E	331,840	p5(L2/3)	p5v1	423	8.2	78.7	261,120
			p5(L5/6)	p5v2	1078	2.2	21.3	70,720
	L5I	72,864	b5	i5	283	1.0	42.9	31,227
			nb5	i5	283	1.3	57.1	41,637
6	L6E	317,424	p6(L4)	p6	456	7.5	75.1	238,506
			p6(L5/6)	p5v1	447	2.5	24.9	78,918
	L6I	65,008	b6	i5	283	1.0	50.0	32,504
			nb6	i5	283	1.0	50.0	32,504

bins have indices $k \in \{0, 1, \dots, K-1\}$, spanning time points in $t \in [k\Delta t, (k+1)\Delta t)$.

Spatiotemporal binning of spike trains

In order to compute the propagation speed of evoked activity in the network, we perform a spatiotemporal binning operation of spiking activity in the network. As introduced in the Section [Point-neuron networks](#), neuron positions (x_i, y_i) of the point-neuron network are randomly drawn with $\{x_i, y_i\} \in [-L/2, L/2)$. We subdivide the spatial domain of each layer into square bins of side length Δl such that the integer numbers of bins along the x - and y -axis are $L_{\{x,y\}} = L/\Delta l$. The bin indices are $l_{\{x,y\}} \in \{0, 1, \dots, L_{\{x,y\}}-1\}$, spanning $\{x, y\} \in [l_{\{x,y\}}\Delta l - L/2, (l_{\{x,y\}} + 1)\Delta l - L/2)$. Temporal bins of width Δt are defined as above. We compute for each population a spatially and temporally binned instantaneous spike-count rate in units of s^{-1} as the number of spike events from all neurons inside the spatial bin divided by Δt .

Calculation of the LFP

The LFP is here defined as the temporally downsampled extracellular signal predicted using the hybrid scheme described in the Section [The hybrid scheme for modeling extracellular signals](#), at a resolution of Δt . Our workflow uses the `decimate` function of the `scipy.signal` package for downsampling by a factor $\Delta t/h$.

Calculation of the CSD

The scheme calculates the CSD from the sum of transmembrane currents within a cuboid around the contact point of each electrode, divided by the corresponding volume (with unit current per volume). This signal is linearly related to the extracellular potential, but without confounding effects by the conductive medium.

Each CSD domain Ω_k is defined as having side lengths $400\mu m$ in the lateral x - and y -dimensions (same as the electrode separation), and thickness $100\mu m$ along the z -axis, centered around each electrode location. Then, the CSD of each cuboid indexed by k in each population results from compartmental currents as

$$C_{\Omega_k} = \frac{1}{V_{\Omega_k}} \sum_{j=1}^M \sum_{n=1}^{n_{comp}} \begin{cases} I_{jn} & \text{if } I_{jn} \text{ fully inside } \Omega_k \\ I_{jn} \frac{\Delta s_{jn,inside}}{\Delta s_{jn}} & \text{if } I_{jn} \text{ partially inside } \Omega_k \\ 0 & \text{otherwise.} \end{cases}$$

Here, V_{Ω_k} denotes the cuboid volume, Δs_{jn} compartment length as above, and $\Delta s_{jn,inside}$ the length of the portion of the compartment inside Ω_k . For the numerical evaluation we use the class `VolumetricCurrentSourceDensity` provided by the `lfpykit` Python package (lfpykit.readthedocs.io).

Calculation of the MUA signal

For each electrode located in L2/3, we compute a signal representative of the so-called MUA that is obtained from recordings of extracellular potentials by high-pass filtering the signal ($\geq 500\text{Hz}$), followed by signal rectification, temporal smoothing, and downsampling (see, for example, [Einevoll et al. 2007](#)). A biophysical modeling study ([Pettersen et al. 2008](#)) shows that this signal is approximately linearly related to the firing rate of the local population of neurons in the vicinity of the measurement device. Neuron coordinates (x_i, y_i) of the upscaled point-neuron network are randomly drawn on the interval $\{x_i, y_i\} \in [-L/2, L/2)$. We subdivide the layers into square bins of side length $\Delta l_{MUA} = 0.4\text{ mm}$ resulting in 10 bins along the x - and y -axis, respectively. The contact point of each electrode is located at the center of the

respective bin. In the same way we define temporal bins of width Δt and compute for each population a spatially and temporally binned spike-count rate in units of s^{-1} by tallying the spike events of all neurons inside the spatial bin and dividing by the width of the temporal bin Δt . We define the MUA signal as the number of spikes per spatiotemporal bin emitted by populations L2/3E and L2/3I.

Statistical analysis

Spike rasters and rate histograms

In the spike raster diagrams, each dot marks a spike event, and the dot position along the horizontal axis denotes the time of the event. Spike data of different neuron populations are stacked and the number of neurons shown is proportional to the population size. As indicated in the respective figure caption, neurons within each population are either scrambled on the vertical axis of the dot display or sorted according to their lateral x-position.

We compute *population-averaged rate histograms* by deriving the per-neuron spike rates in time bins Δt and units of s^{-1} , averaged over all neurons per population within the center disc of 1 mm^2 . The corresponding histogram shows the rates in a time interval of $\pm 25\text{ ms}$ around the occurrence of a thalamic pulse. Such a display is comparable to the Peri-Stimulus Time Histogram (PSTH, Perkel et al. 1967) that typically shows the spike count summed over different neurons or trials versus binned time.

Image plots with color bars can have a linear or a logarithmic scaling as specified in the respective captions. Since values of the distance-dependent cross-correlation functions can be positive or negative, we plot these with linear scaling up to a threshold, beyond which the scaling is logarithmic.

Statistical measures

Per-neuron spike rates FR are defined as the number of spikes per neuron during each simulation divided by the model time T_{model} . Distributions of per-neuron spike rates are computed from all spike trains of each population separately for an interval from 0 to $10s^{-1}$ using 30 bins. Histograms are scaled such that the maximum bar height equals unity. We define the mean rate per population \overline{FR} as the arithmetic mean of all per-neuron spike rates of each population.

The *coefficient of local variation LV* is a measure of spike-train irregularity computed from a sequence of length n of consecutive inter-spike intervals T_i (Shinomoto et al. 2003, Equation 2.2), defined as

$$LV = \frac{1}{n-1} \sum_{i=1}^{n-1} \frac{3(T_i - T_{i+1})^2}{T_i + T_{i+1}}. \quad (24)$$

Like the conventional coefficient of variation CV (Shinomoto et al. 2003, Equation 2.1), a sequence of intervals generated by a stationary Poisson process results in a value of unity, but the LV statistic is less affected by rate fluctuations compared to the CV; thus, a non-stationary Poisson process should result in $LV \approx 1$. We compute the LV from the inter-spike intervals of the spike trains of all neurons within each population. Distributions of LVs are computed from 0 to 2 using 30 bins, and histograms are scaled such that the maximum bar height equals unity. We define the mean LV per population \overline{LV} as the arithmetic mean of all LVs of each population.

The *Pearson (product-moment) correlation coefficient CC* is a measure of synchrony that is defined for signals $u(t)$ and $v(t)$ as

$$CC = \frac{\text{cov}(u, v)}{\sqrt{\text{cov}(u, u) \text{cov}(v, v)}}, \quad (25)$$

with the covariance denoted by *cov* (Perkel et al. 1967). For the numerical evaluation of correlation coefficients we use `numpy.corrcoef`.

To compute distributions of spike-count correlations, $u(t)$ refers to the number $n_i(t, t + \Delta t_{CC})$ of spikes of neuron i in population X and $v(t)$ to the number $n_j(t, t + \Delta t_{CC})$ of spikes of neuron j in population X in a time interval $[t, t + \Delta t_{CC})$. The time window $\Delta t_{CC} = 2\text{ ms}$ corresponds to the refractory time, if not stated otherwise. We randomly select 512 neurons per population and obtain the CC from all disjoint neuron pairs ij . The CC histogram bin width is determined such that the interval from -0.02 to 0.02 is covered by 30 bins, and the histograms are scaled such that the maximum bar height equals unity.

Cross-correlation functions are evaluated for time lags τ . The sequences are spike trains resampled to time steps of Δt and normalized by subtracting their mean and dividing by their standard deviation. Correlation functions between the sequences u and v with time steps k and the length of the sequences K are then computed as

$$CC_{uv}(\tau) = \frac{1}{K} \sum_{k=1}^K u_{k+\tau} v_k. \quad (26)$$

In each layer, we randomly select 512 neurons per population and compute their pair-wise cross-correlation functions (excluding autocorrelations), denoted here by CC^s , for time lags $\tau \in [-25, 25]\text{ ms}$ within each population (indicated by $E : E$ for an excitatory population or $I : I$ for an inhibitory population) and between neurons from the excitatory and inhibitory population (indicated by $E : I$). These correlations are computed using `scipy.signal.correlate`, which is an efficient FFT-based implementation.

The effect of thalamic pulses is analyzed by means of *distance-dependent cross-correlation functions*. These are a function both of the time lag τ and the distance r . We discretize the network of size $L \times L$ into an even number of square bins of side length Δl . The spike trains from all neurons within each spatial bin are resampled into time bins of size Δt (as above) and averaged across neurons to obtain spatially and temporally resolved per-neuron spike rates. We select spatial bins on the diagonals of the network such that each distance to the center with coordinates $(0, 0)$ is represented by four bins. For 14 distances from consecutive spatial bins along the diagonal, we compute the temporal correlation function between the rates in the respective spatial bins with a binary vector containing ones at spike times of the thalamic pulses and zeros elsewhere, and then average over the four spatial bins at equal distance. The cross-correlation functions are then computed according to Equation (26), here evaluated with `np.correlate`. Finally, we subtract the baseline correlation value, obtained by averaging over all negative time lags (before thalamic activation at $\tau = 0$), and get CC^v .

To estimate the *propagation speed* v_{prop} from these cross-correlation functions, we find for each distance the time lag corresponding to the largest CC^v . Values of CC^v smaller than 5 % of the maximum of all CC^v per population across distances and time lags are excluded. We further exclude distances smaller

than the thalamic radius R_{TC}^{pulse} plus the spatial width of thalamic projections σ_{TC} because a large part of neurons within this radius are simultaneously receiving spikes directly from thalamus upon thalamic pulses. A linear fit for the distance as function of time lag, $r_p(\tau) = r_{p,0} + v_{\text{prop}} \cdot \tau$, yields the speed v_{prop} .

We also compute distance-dependent spike-count correlations for spike counts from excitatory and inhibitory spike trains sampled from L2/3 and plot a subset of 512 in each population according to distance between neuron pairs. To assess distance-dependent correlations between LFP, CSD, and MUA signals, u and v denote the time series recorded at the respective electrode. Here, we fit exponential functions of the form

$$y(r) = a \cdot e^{-r/b} + c, \quad (27)$$

where the n -tuple $\beta = (a, b, c)$ of constant parameters minimizes the sum $\sum_{i=1}^m |y_i(r_i) - y(r_i, \beta)|^2$ for the m data points y_i computed for distance r_i . The parameter fitting is implemented using a non-linear least-squares method (Vugrin et al. (2007), using the implementation `curve_fit` of the `scipy.optimize` module), with initial guess $\beta = (0.1, 0.1, 0.1)$. Goodness of fit is quantified by the coefficient of determination, defined as

$$R^2 = 1 - \frac{\sum_{i=1}^m (y_i(r_i) - y(r_i, \beta))^2}{\sum_{i=1}^m (y_i(r_i) - \bar{y})^2}, \quad (28)$$

where \bar{y} is the mean of the observed data.

Coherences are computed as

$$\gamma_{uv}^2(f) = \frac{|S_{uv}(f)|^2}{S_{uu}(f)S_{vv}(f)}, \quad (29)$$

where $S_{uv}(f)$ is the cross-spectral density between u and v , and $S_{uu}(f)$ and $S_{vv}(f)$ are the PSDs of each signal. The cross-spectral density and power spectra are computed using Welch's average periodogram method (Welch 1967) as implemented by `matplotlib.mlab's csd` and `psd` functions, respectively, with segment length $N_{\text{FFT}} = 512$, overlap between segments $N_{\text{overlap}} = 384$ and signal sampling frequency $F_s = 2$ kHz. To compute the population-rate PSD, we use the spike trains of all neurons per population, resampled into bins of size Δt , and with the arithmetic mean across time of this population-level signal subtracted.

Software accessibility

We here summarize the details of software and hardware used to generate the results presented throughout this study. Point-neuron network simulations are implemented using NEST v3.8 (Graber et al. 2024), and Python v3.11.3. We use the same executable model description for the reference and upscaled models and switch between them by adjusting parameters. LFP signals are computed using NEURON v8.2.2 (branch 'master' at SHA:93d41fafd), LFPykit v0.5 (<https://github.com/LFPy/LFPykit.git>, branch 'master' at SHA:e5156c0) and LFPy v2.3.1.dev0 (<http://github.com/LFPy/LFPy.git>, branch 'master' at SHA:5d241d6), hybridLFPy v0.2.1 (<https://github.com/INM-6/hybridLFPy>, branch 'espenhgn/issue84' at SHA:0be2961). For parameter evaluation we use the Python package parameters v0.2.1. Analysis and plotting rely on Python with numpy v1.25.1, SciPy v1.11.1, and matplotlib v3.7.2. All simulations and analyses are conducted on the JURECA-DC cluster (Thörnig 2021). Simulations are run distributed using 16 compute nodes with two AMD EPYC 7742 CPUs à 64 cores each for both the network and the LFP simulations. All source

codes to reproduce our results are publicly available on GitHub (<https://github.com/INM-6/mesocircuit-model>) and on Zenodo (<https://doi.org/10.5281/zenodo.13798935>). Further, all simulation outputs and scripts needed to generate the manuscript figures are available on Zenodo (<https://doi.org/10.5281/zenodo.13799065>).

Results

Spiking activity of the point-neuron networks

After the description and parameterization of the reference and the upscaled models in the Section [Point-neuron networks](#), we here investigate their spiking activity obtained by direct simulation. In the Section [Spontaneous activity](#) we compare the spontaneous spiking activity of both models, and in the Section [Sensitivity to perturbed parameters during evoked activity](#) we investigate the response evoked by a transient thalamocortical activation in the upscaled model. Our main objective is to confirm that the upscaling procedure preserves the overall statistics of the reference model, and that the inclusion of space facilitates activity propagating across lateral space.

Spontaneous activity

The spike raster plot in Fig. 3A and the population-averaged rate histograms in Fig. 3C show that the reference model produces asynchronous irregular spiking with firing rates below 10 spikes/s (Softky and Koch 1993; Brunel and Hakim 1999; Brunel 2000) and rate fluctuations comparable in amplitude to the mean rate for each population. The firing rates are on average higher for inhibitory populations than for excitatory populations within the same layer, and the mean firing rate is larger than the median for each population (see Fig. 4A). The latter corresponds to the long-tailed distributions of spike rates in Fig. 4D with most neurons firing at lower rates. This type of asymmetric distribution of firing rates in the model resembles the lognormally distributed firing rates observed experimentally (reviewed by Buzsáki and Mizuseki 2014). The mean values of the coefficients of local variation (Fig. 4B,E) are close to unity, indicating that the regularity of the spike trains is similar to that of a Poisson point process ($LV = 1$). The distributions are broad, that is, a fraction of neurons in each population has spike-train statistics with $LV > 1$. The mean LV values are comparable to values observed in visual cortex across different species (Mochizuki et al. 2016, Figure 5B). The box plots in Fig. 4A,B are similar to (Potjans and Diesmann 2014, Figure 6) showing firing rates and the conventional coefficient of variation (Shinomoto et al. 2003, Equation 2.1). The Pearson correlation coefficients (CC, Fig. 4C,F) are distributed around zero. With our model time of $T_{\text{model},1} = 15$ min, the shapes of the distributions observed here are not strongly affected by the finite simulation duration, but they are not fully converged yet. The effects of simulation duration were investigated by Dasbach et al. (2021) using the microcircuit model by Potjans and Diesmann (2014) (see Figures 2 and 7 of Dasbach et al. 2021). We here use the same maximum duration as they. Weak pairwise spike-train correlations (with mean values < 0.1 using 50 ms count windows) are reported, for example, by Ecker et al. (2010), who record from nearby neurons in primary visual cortex of awake monkey under different stimulation conditions. The population-rate PSDs in Fig. 4G show that the power tends to be higher in the activity of excitatory compared to inhibitory populations in each layer due to the overall larger density of excitatory neurons, except for layer 2/3, where the excitatory rate is less than 1 spike/s. Across layers, the power is highest in layer 4, explained by the comparatively

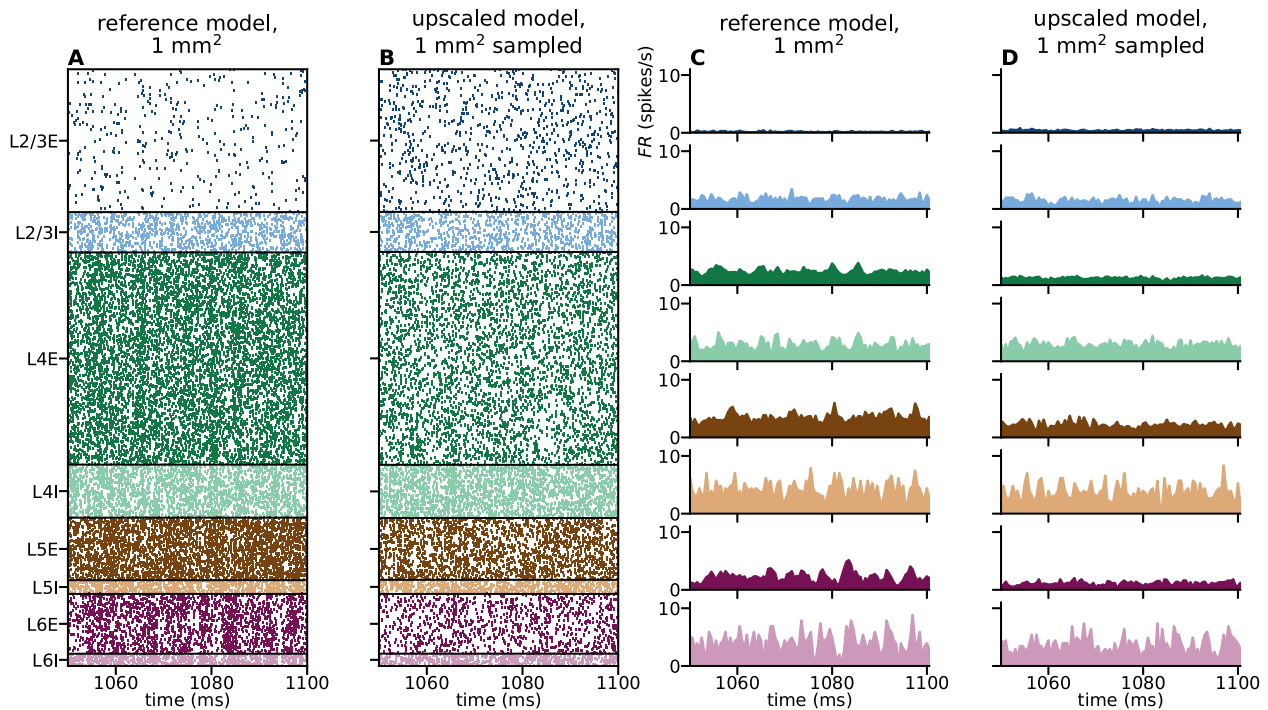


Fig. 3. Spike raster plots and instantaneous firing rates. Spike times are vertically organized according to populations defined by layer and neuron type. **A** Spikes of all neurons of the 1 mm² reference model. **B** Spikes of all neurons located within a center disc of 1 mm² in the upscaled model. Neuron IDs within each population are randomized; spatial information is scrambled. **C** Population-averaged rate histogram with temporal bin size $\Delta t = 0.5$ ms of spike data in panel A. **D** Population-averaged rate histogram with temporal bin size Δt of spike data in panel B.

high spike rates and high cell densities. The power spectra are relatively flat without visible dominant oscillation frequencies.

Analyzing the spike data of all neurons of the upscaled model that are located within the central disc of 1 mm² yields qualitatively similar spiking statistics to the reference model, as seen by comparing Fig. 3 panels A,C versus panels B,D and Fig. 4 panels A–G versus H–N. The difference between inhibitory and excitatory firing rates in each layer is more pronounced in the upscaled model. The upscaled model also exhibits an increased excitatory firing rate in layer 2/3 compared to the reference model and reduced excitatory firing rates in the other layers. Fig. 5 provides a closer look on the spike train correlations of the upscaled model: Wider count windows lead to wider distributions of Pearson correlation coefficients while the mean remains close to zero (see panel A). The spike-count cross-correlation functions in panel B indicate that the structured part of the cross-correlations in our model indeed only spans time lags of at most a few milliseconds; for the corresponding theory, refer to Renart et al. (2010); Tetzlaff et al. (2012); Helias et al. (2014).

The scaling factors for recurrent and external in-degrees (k_{yx} and $k_{ext,y}$ in Table 4) are chosen based on a dynamic argument: There is accumulating evidence that the typical operating regime of sensory cortices is asynchronous and irregular in particular in the awake state when no specific stimulus is present. Measures of LFP signals, which are assumed to mainly reflect synaptic activity, in, for example, visual cortex also do not show pronounced peaks in their spectra in the absence of stimuli (see, for example, Berens et al. 2008; Jia et al. 2011; Ray and Maunsell 2011a; Jia et al. 2013a; Kerkoerle et al. 2014). The reference model already shows reduced global synchrony in the low- and high-gamma ranges compared to the model by Potjans and Diesmann (2014), but some spontaneously occurring, coordinated rate fluctuations are visible (Fig. 3A). We apply the mentioned perturbations to the

in-degrees in order to achieve asynchronous-irregular activity at plausible firing rates with further attenuated rate fluctuations in the final upscaled model. Our approach is informed by the analytical framework by Bos et al. (2016) who provide a sensitivity measure that relates population rate spectra to the connectivity of the underlying neuron network. Since the in-degrees in the reference model are estimated across different areas and species and are merely suggestive of typical cortical connectivity, we consider modifications to these values to be within the bounds of uncertainties. In-degree values can be refined in future model iterations when further experimental connectivity data becomes available.

In the rate power spectra of the upscaled model (Fig. 4N), we observe a peak at ~ 50 Hz across all populations except within layer 4 where such oscillations are attenuated via the increased in-degree from L4I onto itself, leaving only a shoulder and peak above ~ 100 Hz for L4E and L4I respectively. The low-gamma peak seen around 50 Hz is predominantly generated by a sub-circuit of layer 2/3 and layer 4 populations of excitatory and inhibitory neurons (pyramidal-interneuron gamma or PING mechanism (Leung 1982; Börgers and Kopell 2003, 2005; Bos et al. 2016). A high-gamma peak $\gtrsim 200$ Hz resulting from interneuron-interneuron interactions (interneuron-interneuron gamma mechanism, see Whittington et al. 1995; Wang and Buzsáki 1996; Chow et al. 1998; Whittington et al. 2000) is pronounced in the version of the microcircuit model by Potjans and Diesmann (2014) studied by Bos et al. (2016) but not in the reference model. See Buzsáki and Wang (2012) for a review on the various mechanisms underlying gamma oscillations.

Sensitivity to perturbed parameters during evoked activity

We have so far only considered networks receiving external inputs with stationary rates. However, cortical areas are recurrently

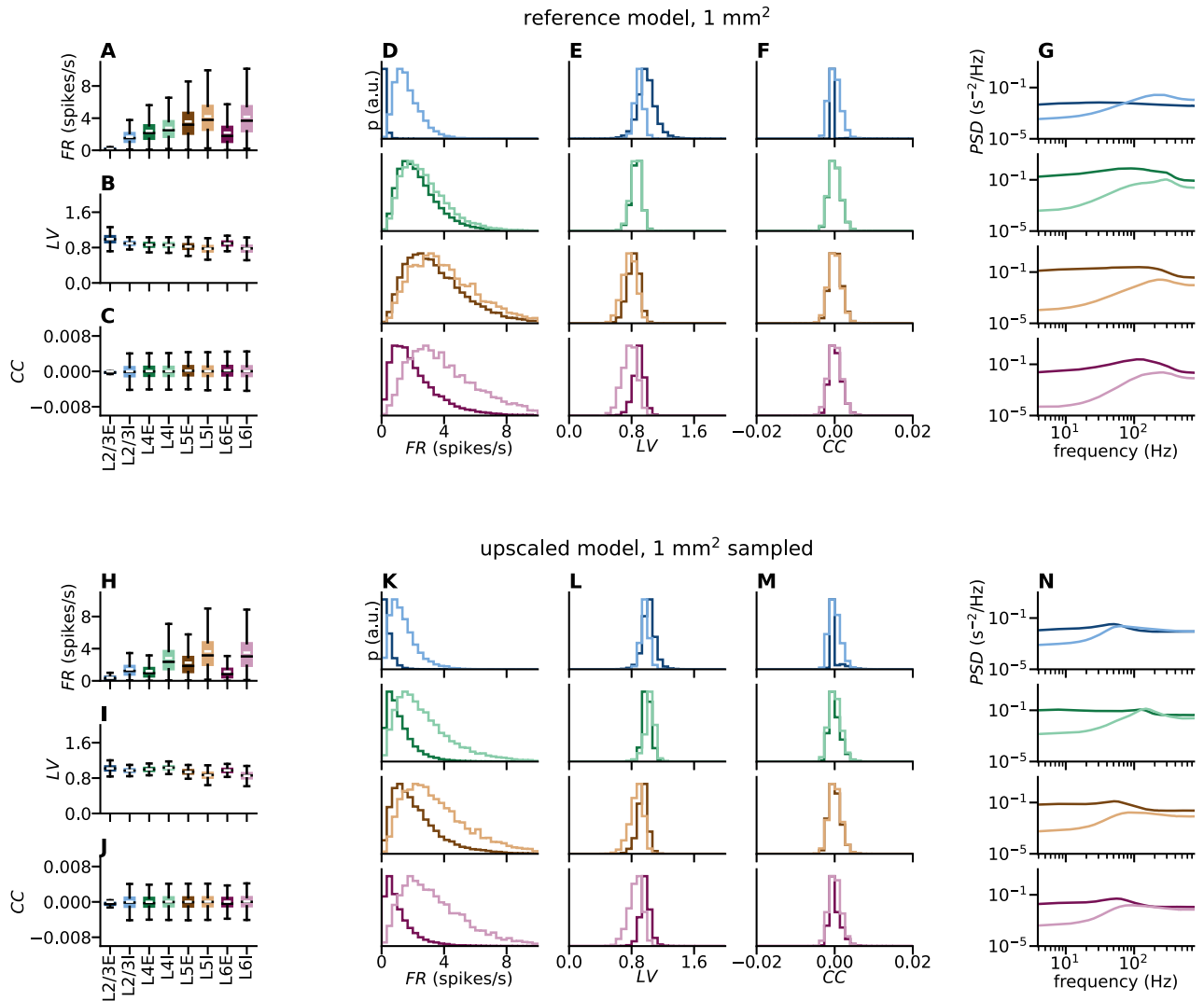


Fig. 4. Statistical analysis of the spike data shown in Fig. 3. Data of full simulation duration $T_{\text{model},1}$ analyzed for reference model (top, panels A–G, 1 mm^2) and upscaled model (bottom, panels H–N, 1 mm^2 sampled). **A, H** Box plots (Tukey 1977) of spike rates FR for each population (horizontal black lines: median, white lines: mean, boxes in population-specific colors: lower and upper quartiles of the data, whiskers extend to most extreme observations within $1.5 \times \text{IQR}$ beyond the IQR (interquartile range) without outliers (created with matplotlib.pyplot.boxplot). **B, I** Coefficients of local variation LV, see Equation (24). **C, J** Pearson correlation coefficients CC, see Equation (25). **D, K** Distributions of spike rates FR. **E, L** Distributions of coefficients of local variation LV. **F, M** Distributions of Pearson correlation coefficients CC. **G, N** Population-rate PSD.

connected to other parts of cortex and subcortical structures, and receive inputs with large rate fluctuations. In order to assess the speed of evoked wave propagation across cortical space, we here mimic a stimulation experiment, by activating all thalamic neurons inside a disc of radius $R_{\text{TC}}^{\text{pulse}}$ centered around $(x, y) = (0, 0)$ once every time interval of Δt_{TC} (see Table 4 for values). The activation could, for example, represent a visual stimulation experiment where activity in lateral geniculate nucleus (or visual thalamus) thalamocortical (TC) projection neurons is evoked by a brief flash stimulus to a part of the visual field (Bringuier et al. 1999; Muller et al. 2014), air puffs or mechanical whisker deflections to stimulate whisker barrel cortex (Swadlow et al. 2002; Einevoll et al. 2007), or direct electric or optogenetic stimulation of the thalamocortical pathway (Klein et al. 2016). The model of Potjans and Diesmann (2014, page 802) exhibits a *handshake principle* in response to thalamic pulses due to mutual interactions of excitatory and inhibitory populations, in which the receiving layer inhibits the sending layer as if to signal that it has received the message, so that the sending layer can stop

transmitting. We test whether this mechanism is preserved in the upscaled model. Furthermore, we derive the propagation speed of evoked spiking activity spreading outward from the center of stimulation.

Figure 6A shows series of snapshots of spatiotemporally binned activity of each population in the full network of size $4 \times 4 \text{ mm}^2$ (similar to Mehring et al. 2003; Yger et al. 2011, Figure 2). The thalamic pulse is visible at $t = 1, 100 \text{ ms}$ in the center of the network. The cortical populations respond with a ring-like outward spread of activity that can be described as a traveling wave, in contrast to a stationary bump of activity (Muller et al. 2018). The spike raster in Fig. 6B sorts the neurons within each population vertically according to their x -position: the activity before the pulse appears to be asynchronous and irregular, and the spatially confined outward spread of high activity caused by the pulse is followed by reduced activity for tens of milliseconds across different populations until the asynchronous-irregular activity is reattained. In Hao et al. (2016, Figure 3) a similar suppression period of tens of milliseconds is observed after a single-pulse

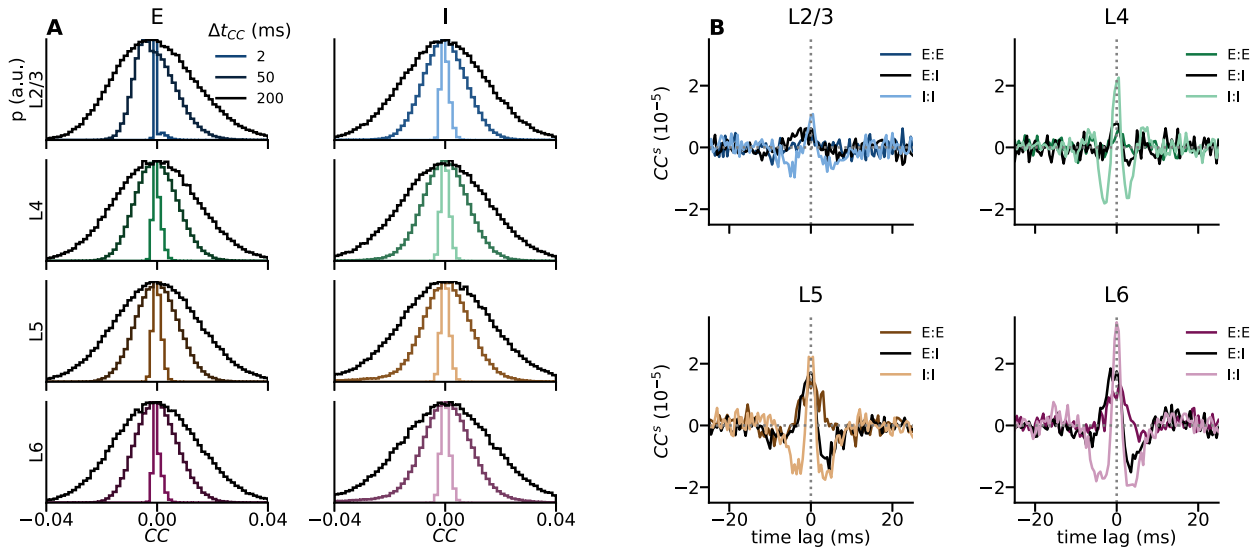


Fig. 5. Cross-correlation analysis of the spike data shown in Fig. 3 for the upscaled model. **A** Distributions of pairwise Pearson correlation coefficients CC computed with different time windows Δt_{cc} . The data displayed for $\Delta t_{cc} = 2$ ms is the same as in Fig. 4M. **B** Mean pairwise spike-count cross-correlation functions for each layer.

electrical micro-stimulation in monkey motor cortex, often followed by a rebound of excitation. The population-averaged rate histograms in Fig. 6 highlight the transient network responses. The strong initial response visible in populations L4E and L6E is expected since the thalamocortical input targets layers 4 and 6 directly (see Table 4). This evoked activity affects the other network populations via recurrent connections across and within layers. The duration of the activation is overall similar to evoked MUA following whisker stimulation as reported by Einevoll et al. (2007). The multiple peaks in the rate histograms in panel C, most prominent in populations L4E and L6E, are due to recurrent excitation and inhibition within and across layers. These results are comparable with Potjans and Diesmann (2014, Figure 10) and Hagen et al. (2016, Figure 7), and we therefore conclude that the upscaling procedure does not fundamentally affect the response of the network to transient external input apart from introducing spatial structure.

In order to derive the radial propagation speed of evoked activity, we compute the distance-dependent cross-correlation functions (see Section Statistical measures) shown in Fig. 6D. The propagation speed v_{prop} is computed separately for each population via the shift of the maximum value of $CC^*(\tau, r)$ for time lags τ with increasing distance r . It is to date difficult to observe wave-like activity on the spiking level (Takahashi et al. 2015). However, model predictions for spiking propagation speeds can be compared with other measures, keeping in mind potential differences between spiking activity and population measures such as the LFP. Both types of signals can reflect propagation along long-range horizontal connections (Grinvald et al. 1994; Nauhaus et al. 2009; Takahashi et al. 2015; Zanos et al. 2015), which also includes synaptic processing times, but they are also affected by intrinsic dendritic filtering (Lindén et al. 2010). Muller et al. (2018) remark that macroscopic waves traveling across the whole brain typically exhibit propagation speeds of 1–10 mm/ms, similar to axonal conduction speeds of myelinated white matter fibers in cortex, while mesoscopic waves (as considered here) show propagation speeds of 0.1–0.8 mm/ms, similar to axonal conduction speeds of unmyelinated long-range horizontal fibers within the superficial layers of cortex. For example, LFP signals

and signals obtained with voltage-sensitive dye imaging in visual cortex propagate with similar speeds, see Table 7. Estimates from monkey motor cortex are in the same range (Rubino et al. 2006; Takahashi et al. 2015; Denker et al. 2018). The derived propagation speeds in our model are $v_{prop} \in [0.13, 0.17]$ mm/ms, which is within the range of experimentally measured propagation speeds. Note that these values are smaller than the fixed conduction speed ($v = 0.3$ mm/ms) because propagation through the network includes neuronal integration and the delay offsets.

Prediction of extracellular signals

We here summarize our findings for the calculated LFP, CSD and MUA signals across the cortical space spanned by the upscaled network model, with recording geometry similar to a 4×4 mm² Utah multi-electrode array. As in Hagen et al. (2016), the eight cortical network populations spanning layers 2/3, 4, 5 and 6 are expanded into 16 different cell types to account for differences in laminar profiles (layer specificities) of synaptic connections among cell types in a single layer when predicting the LFP. The detailed derivation of laminar profiles from the anatomical data (i.e. Binzegger et al. 2004) is given in Hagen et al. 2016 (but see Section The hybrid scheme for modeling extracellular signals). In Fig. 7 we show the reconstructed morphology used for each cell type y in population Y , with occurrences and compartment counts summarized in Table 6. The cortical layer boundaries and depths are also shown in the figure, and each morphology is positioned such that the soma is at the center of the corresponding layer. Different cell types belonging to the same population within a layer may have different geometries supporting different laminar profiles of synaptic connections. For example, the p4 pyramidal cell type and the ss4 spiny stellate cell types both belong to population L4E of the point-neuron network. Previous modeling studies demonstrate the major effect of the geometry of the morphology on the measured extracellular potential due to intrinsic dendritic filtering of synaptic input (e.g. Lindén et al. 2010, 2011; Łęski et al. 2013), which is also accounted for here.

The geometry of the recording locations corresponding to the 4×4 mm² Utah multi-electrode array is illustrated in Fig. 8A. Fig. 8B shows example LFP signal traces corresponding to the

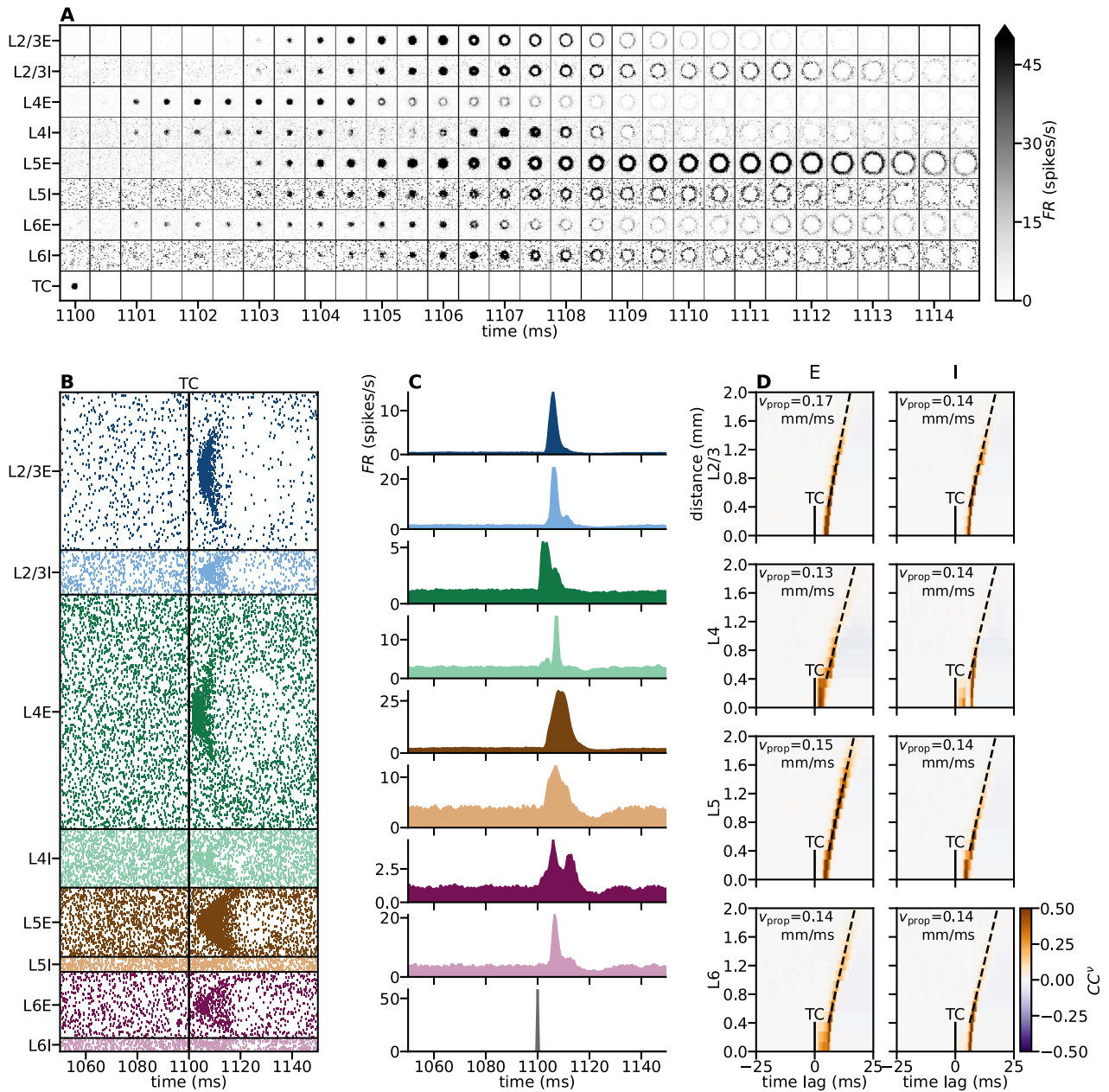


Fig. 6. Activity evoked by thalamic pulses. **A** Series of snapshots of spatiotemporally binned activity per population over the whole $4 \times 4 \text{ mm}^2$ network. **B** Spike raster showing every 25th neuron of all neurons in $4 \times 4 \text{ mm}^2$; neurons are sorted according to their x-position. The network is stimulated by a single thalamic pulse at $t = 1, 100 \text{ ms}$. **C** Population-averaged rate histograms with temporal bin size $\Delta t = 0.5 \text{ ms}$ for a time interval around the thalamic pulse. **D** Distance-dependent cross-correlation functions $CC^*(\tau, r)$ between thalamic activation (length of vertical bar indicates radius of patch of active thalamic neurons) and spatially binned spiking activity, where r is the distance to the center of the network and τ is the time lag. Estimate for wave propagation speed v_{prop} through linear fit (dashed line).

spontaneous activity in our laminar, upscaled point-neuron network, with spike raster plot shown in Fig. 3B. The LFP signal fluctuates with amplitudes somewhat smaller than experimentally observed spontaneous potentials ($0.1 - 1 \text{ mV}$, Maier et al. 2010; Hagen et al. 2015; Reyes-Puerta et al. 2016; Rimehaug et al. 2023), with occasional transients above $50 \mu\text{V}$ (occurring outside shown interval). This result is expected as there are no external sources of rate fluctuations and associated LFPs such as thalamic activation or feedback from other areas, which may otherwise explain larger signal amplitudes. The amplitudes observed here are also smaller than those from the forward-model predictions of LFPs from spontaneous activity in a 1 mm^2 network model (Potjans and Diesmann 2014; Hagen et al. 2016, Figure 8M),

although the total number of neurons in the upscaled model is greater by a factor of ~ 40 . The discrepancy is explained by strong gamma oscillations generated in the 1 mm^2 network model (Hagen et al. 2016).

For comparison with the LFP, we show in Fig. 8C the corresponding CSD signal computed from transmembrane currents in the same locations. The LFP and corresponding CSD in general reflect correlations in synaptic input nearby the measurement site and therefore contain contributions from both local and remote neuronal activity (Kajikawa and Schroeder 2011; Lindén et al. 2011; Łęski et al. 2013; Rimehaug et al. 2023). The CSD reflects the gross in- and outgoing transmembrane currents in vicinity to the recording device (Nicholson and Freeman 1975;

Table 7. Comparison of selected model results with experimental data.

Activity results		
Propagation speed in visual cortex (upscaled model: $v_{\text{prop}} \in [0.13, 0.17]$ mm/ms)		
Value (mm/ms)	Data acquisition	Reference
0.31 ± 0.23 (cat)	anesthetized cat and monkey, propagation of spike-triggered LFPs both in spontaneous	Nauhaus et al. (2009)
0.24 ± 0.2 (monkey)	activity and with visual stimulation (mean \pm standard deviation)	
0.18 (cat) 0.29 (monkey)	reanalyze the data from Nauhaus et al. (2009), impulse response of ongoing activity	Nauhaus et al. (2012)
0.13	awake monkey, LFP	Ray and Maunsell (2011b)
0.31 ± 0.08	monkey, LFP propagation triggered by saccades (mean \pm standard deviation)	Zanos et al. (2015)
0.1 – 0.25	monkey, voltage-sensitive dye imaging	Grinvald et al. (1994)
0.28 [0.19, 0.55]	cat, voltage-sensitive dye imaging (mean and 75% confidence interval)	Benucci et al. (2007)
$0.25 - 1.35$ (0.57 ± 0.18)	monkey, voltage-sensitive dye imaging (range and median \pm standard deviation)	Muller et al. (2014)

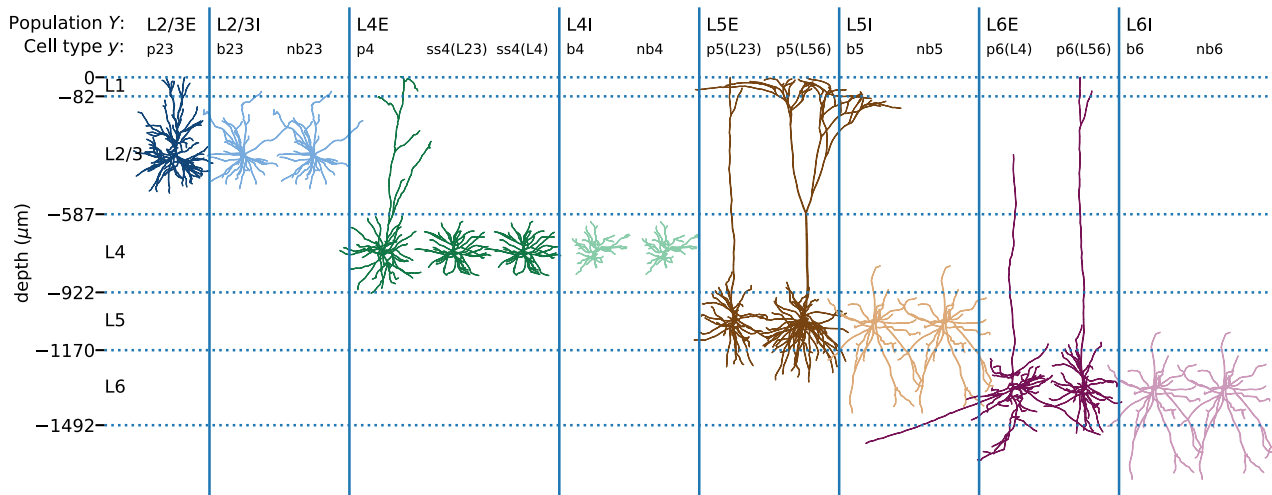


Fig. 7. Cell types and morphologies of the multicompartment-neuron populations. The 8 cortical populations Y in the 4×4 mm² network model are represented by 16 subpopulations of cell type y with detailed morphologies (Binzegger et al. 2004; Izhikevich and Edelman 2008). Neuron reconstructions are obtained from cat visual cortex and cat somatosensory cortex (source: NeuroMorpho.org by Kisvárdy and Eysel (1992), Mainen and Sejnowski (1996), Contreras et al. (1997), Ascoli et al. (2007), and Stepanyants et al. (2007); see Hagen et al. 2016, Table 7). Each morphology is here shown in relation to the layer boundaries across depth (horizontal lines). Colors distinguish between network populations as in Fig. 1.

Mitzdorf 1985; Pettersen et al. 2006, 2008; Potworowski et al. 2012), and is therefore expected to be less correlated across space than the LFP, which is affected by volume conduction. Thus on average, LFP traces from neighboring sites are more correlated than sites further apart, detailed in the Section [Distance-dependent correlations of spike trains and LFPs](#).

The high-frequency ($\gtrsim 100$ Hz) part of experimentally obtained extracellular potentials contains information on spiking activity of local neurons (see e.g. Einevoll et al. 2012). Spikes of single neurons may be extracted from the raw signal based on classification of extracellular waveforms of the action-potentials (through *spike sorting*, Quiroga 2007; Einevoll et al. 2012). Even if no units are clearly discernible in the high-frequency part of the signal, a previous forward-modeling study using biophysically detailed neuron models (Pettersen et al. 2008) shows that the envelope of the rectified high-pass filtered (750 Hz cutoff frequency) signal correlates well with the spike rate in the local population of neurons. Pettersen et al. (2008) refer to this rectified signal as the MUA, which we approximate by summing up the spiking activity of layer 2/3 neurons in 400×400 μm^2 spatial bins around each contact and weighting the contributions from excitatory and inhibitory neurons identically. Consequently MUA signals have more high-frequency content than the LFP and CSD signals at the same

locations (Fig. 8D). To quantify this observation, we next compare the power spectra.

Signal power spectra

As a first quantitative inspection of the different virtual measurements of network activity, we compute the mean PSDs of LFP, CSD, and MUA signals and their standard deviations in all channels (Fig. 8E–G). The population firing rate spectra exhibit a gamma oscillation around 50 Hz (Fig. 4N). The oscillation is prominent in the MUA spectra, due to MUA directly reflecting the firing rates in L2/3. LFP and CSD express the gamma oscillation merely as a shoulder in the respective PSD. Above ~ 50 Hz, the signal power of the LFP and CSD decay steeply (approximately as $1/f^2$), mainly explained by the combination of intrinsic dendritic filtering (Lindén et al. 2010) and synaptic filtering from using exponential temporal kernels for the synaptic currents. This low-pass filtering effect is absent in the population firing rates and in the MUA signal PSD, which flattens out toward higher frequencies. At frequencies $\lesssim 50$ Hz, the LFP and CSD increase in power down to ~ 10 Hz, below which their spectra remain comparatively flat, in contrast to the attenuated low frequency content in the MUA. Monotonically decreasing LFP signal amplitudes with frequency

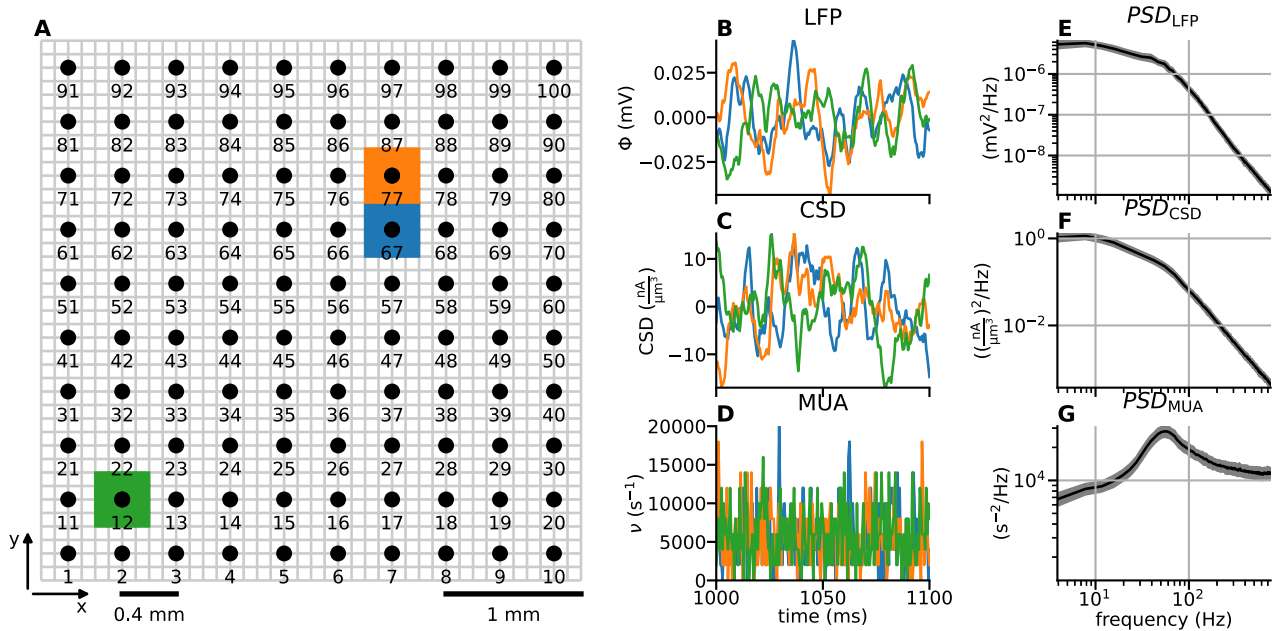


Fig. 8. Top-down illustration of multi-electrode array geometry and LFP, CSD, and MUA signals. **A** Extracellular potentials are computed in 10×10 electrode locations denoted by circular markers at the depth corresponding to the center of layer 2/3. The electrode inter-contact distance is $400 \mu\text{m}$. The signals are computed at the center of layer 2/3 (at $z = -334 \mu\text{m}$). The number under each circular marker denotes the channel number. **B–D** LFP, CSD, and MUA signal excerpts from three chosen contacts numbered 12, 67, and 77, color code as in panel A. The CSD is computed from transmembrane currents, and the MUA is calculated as the count of excitatory and inhibitory spike events from layer 2/3 neurons in spatiotemporal bins of duration $\Delta t = 0.5 \text{ ms}$ and width $400 \mu\text{m}$ around each contact. The pairwise correlations between these signals computed for the full 5 s simulation duration are: LFP: $CC_{\text{ch.67:77}} = 0.37$, $CC_{\text{ch.12:67}} = 0.068$, $CC_{\text{ch.12:77}} = 0.024$; CSD: $CC_{\text{ch.67:77}} = 0.040$, $CC_{\text{ch.12:67}} = -0.093$, $CC_{\text{ch.12:77}} = 0.014$; MUA: $CC_{\text{ch.67:77}} = 0.035$, $CC_{\text{ch.12:67}}^{\text{MUA}} = -0.0027$, $CC_{\text{ch.12:77}}^{\text{MUA}} = -0.011$. **E** LFP power spectrum averaged over channels (black line). The gray area denotes the average spectrum plus/minus one standard deviation computed over all observations. **F, G** Same as panel E, but for the CSD and MUA signals.

are consistent with experimental observations (see, e.g. Jia et al. 2011; Prakash et al. 2021).

The lack of low-frequency power in the MUA is partly explained by the background input with a flat power spectrum (a Poisson process with fixed rate) and the absence of recurrent sub-circuits capable of generating slow rate fluctuations or slow oscillations. One mechanism contributing to the lack of low-frequency power in the MUA is active decorrelation by inhibitory feedback, which suppresses population-rate fluctuations (Tetzlaff et al. 2012; Helias et al. 2014). With LFP power spectra in qualitative agreement with experimental observations, we investigate the properties of these signals in terms of distance-dependent correlations and coherences.

Distance-dependent correlations of spike trains and LFPs

The observation of weak pairwise spike-train correlations in cortical neuronal networks (for example, Ecker et al. 2010) is seemingly at odds with the typical observation of highly correlated LFPs across cortical space (for example, Nauhaus et al. 2009). We have so far established that the mean pairwise spike-train correlations within populations in our spatially organized layered network are typically near zero for spontaneous activity (Section Spontaneous activity). However, the network can propagate waves of synchronous activity when excited by external input (Section Sensitivity to perturbed parameters during evoked activity). Here, we focus on spontaneous activity, as it is unclear how this weakly correlated network activity affects population signals such as the LFP across space. Previous modeling studies highlight the crucial role of correlation in synaptic inputs for the spatial reach of the LFP (Lindén et al. 2011; Łęski et al. 2013). In contrast to these studies, which rely on input spike trains with Poisson inter-spike statistics, we here account for ongoing network interactions, and

full numbers of neurons and connections under $4 \times 4 \text{ mm}^2$ of cortical surface.

For spontaneous spiking activity in the upscaled network, we analyze the LFP, CSD, and MUA across the 100 channel locations in layer 2/3 illustrated in Fig. 8A, with panels B–D showing temporal snapshots of each signal in three different channels. In addition to pairwise spike train correlations computed for a subset of neurons in network populations L2/3E and L2/3I arranged by their separation (Fig. 9A), we compute the Pearson product-moment correlation coefficient between all possible pairs of LFP channels, and sort them by inter-contact distance (Fig. 9B). Due to the periodic boundary conditions of the upscaled network and LFP model, the largest possible separation between contacts is $L/\sqrt{2} \approx 2.8 \text{ mm}$ (i.e. five electrode contacts along the diagonal). The mean values are well fit by a simple exponential function, with a space constant of $\sim 0.53 \text{ mm}$ and an offset of ~ 0.047 . The correlations in the simulated LFP (marginal distribution across all distances in Fig. 9B) are lower compared to findings by Nauhaus et al. (2009, Fig. 8) during spontaneous activity in anesthetized macaque (approximately 0.95 at 0.4 mm and 0.75 at 2.4 mm electrode separation, respectively) and cat (approximately 0.93 at 0.4 mm and 0.83 at 2.4 mm electrode separation, respectively). However, with high-contrast drifting grating type stimuli the correlations between pairs of LFP signals are shown to decrease to values around 0.5 at an electrode separation of 2.4 mm. Also Destexhe et al. (1999) analyze spatial correlations in the LFP of cat suprasylvian cortex during awake and different sleep states, and find mean correlations of approximately 0.6 at 2 mm contact separation in the awake state. The point neuron and corresponding LFP model also ignore rate fluctuations in their background input (here represented as Poisson generators with fixed rates), which may be another source of spatial correlations in vivo. Global

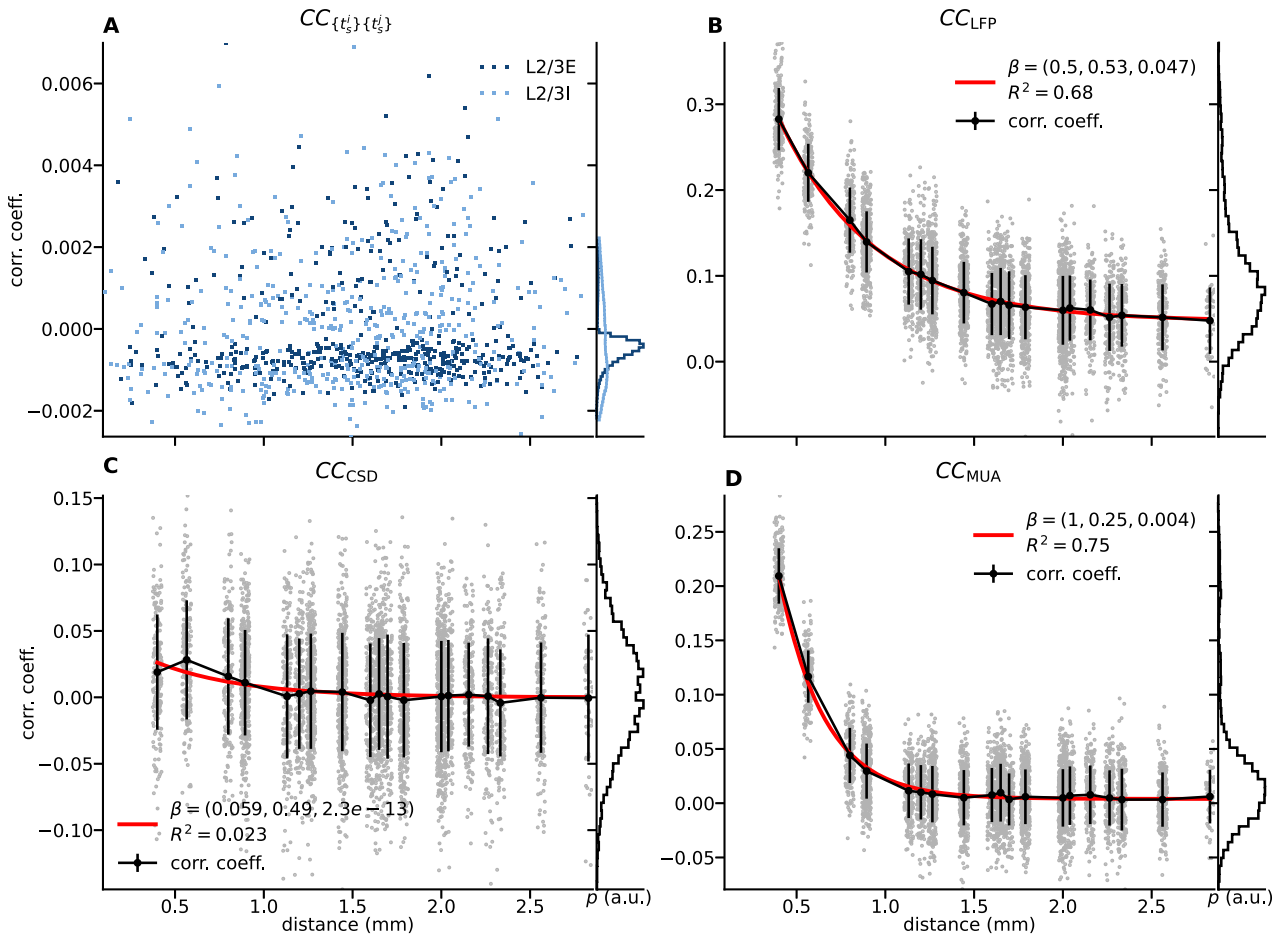


Fig. 9. Distance-dependent correlations in spike trains, LFP, CSD, and MUA signals in L2/3. **A** Pairwise spike–train correlations (vertical) computed for excitatory (E–E, $n = 512$) and inhibitory (I–I, $n = 512$) pairs of L2/3 neurons (color code in legend), sorted by inter-neuron distance r (horizontal) and gathered across all distances as marginal distributions (vertically, right side of panel). The correlations are computed from spike trains of a long duration network simulation ($T_{\text{model},1} = 15$ min). **B** Pearson correlation coefficient between pairs of LFP signals as function of separation between channels. The black curve (denoted “corr. coeff.”) shows the mean at each unique separation (marginal as in panel A); whiskers denote 1 standard deviation. The red curve (denoted with β and R^2) shows the least-squares fit of an exponential function (Equation (27)) to all data points (coefficient of determination (R^2) in legend). **C** Similar to panel B but for CSD signals. **D** Similar to panel B but for MUA signals. Histograms of the values marginalized across distance are given at the right of each panel. Note that the distance values in panels B–D result from the electrode layout (see Fig. 8A); for visibility, the individual data points are jittered along the horizontal axis by adding uniformly distributed random numbers in $[-0.025, 0.025]$.

fluctuations or shared input correlations in the background input can be expected to increase pairwise LFP correlations (Lindén et al. 2011; Łęski et al. 2013; Hagen et al. 2016).

Bringing our attention to CSDs (Fig. 9C), the calculated CSD is expected to suppress correlations among channels due to volume conduction and represents the local sink/source pattern underlying the LFP (Nicholson and Freeman 1975; Mitzdorf 1985; Pettersen et al. 2006, 2008; Potworowski et al. 2012). The overall positive correlations observed for the LFP are mostly gone for the CSD: the correlations are on average only positive at short separations and negligible beyond 1 mm electrode separation. This negligible correlation at greater distances reflects in part that dendrites of each morphology (cf. Fig. 7) are mostly confined within $\sim 300 \mu\text{m}$ in the lateral directions. Also, the CSD estimate (cf. Section Calculation of the CSD) is here computed at a single depth only, but CSDs do vary across depth, mediated mainly by the apical dendrites of the pyramidal cell populations across layers.

The MUA estimate based on the sum of spiking activity in L2/3 in the vicinity of each LFP contact point (cf. Section Calculation of the MUA signal) results in the distance-dependent correlations in Fig. 9D. In contrast to pairwise spike–train correlations (Fig. 9A), a monotonically decaying distance dependence

is observed, which is well fit by an exponential function with spatial decay constant of ~ 0.25 mm and vanishing offset from zero at greater distances. This sharper decay, about half of the spatial decay constant observed for the LFP, reflects the fact that the LFP is essentially composed of spatiotemporally filtered spiking activity. In conclusion, the model reproduces the theoretical result that sums of correlated variables are generally more strongly correlated than the individual components in the sum (Bedenbaugh and Gerstein 1997; Harris and Thiele 2011; Rosenbaum et al. 2011; Tetzlaff et al. 2012), and in addition shows a distance dependence in these composed signals (in particular in the LFP and MUA) similar to experimental findings.

Spatial coherence of local field potential is band-passed

So far we have established that the model LFP is correlated across distance in qualitative agreement with experimental findings, while the corresponding CSD and MUA signals are hardly correlated beyond electrode separations of ~ 1 mm. We next extend this analysis to the frequency domain by considering distance-dependent coherences, mainly motivated by two experimental observations: LFP coherence across channels depends on inter-electrode distance as reported by Jia et al. (2011) and Srinath

and Ray (2014), and a study by Dubey and Ray (2016) showing that the ‘spatial spread’ of LFP has band-pass properties in the gamma range. Another modeling study (Łęski et al. 2013) extends the study of LFP ‘reach’ by Lindén et al. (2011) to distance-dependent coherences, showing that dendritic filtering (Lindén et al. 2010) introduces a low-pass effect on the LFP reach of uncorrelated synaptic input currents with an approximately white power spectrum. In contrast to these latter modeling studies, our combined point-neuron network and LFP-generating setup allows accounting for weakly correlated spiking activity in the network, at realistic density of neurons and connections. In contrast to the earlier model studies, the network’s spiking activity is non-random and the corresponding firing rate spectra is frequency dependent (Fig. 4N), which may allow testing the hypothesis that network activity in the gamma range results in increased coherence in the LFP, explaining the apparent band-pass filter effect.

From the LFP spectrum (Fig. 8E), we infer that a fraction of its variance is due to a low-frequency gamma oscillation around 50 Hz mainly explained by the PING mechanism (detailed in Section Spontaneous activity). In Fig. 10A we show the mean coherences $\langle \gamma_{\text{LFP-LFP}} \rangle(f)$ between individual pairs of LFP signals from channels separated by a distance $r = \{0.4, 0.8, 1.2, 1.6, 2.0\}$ mm. The coherence drops quickly from 0 Hz to around 15 Hz. For the shortest separation (0.4 mm), the coherence is around 0.05 at this frequency, and increases above ~ 0.25 in the low-gamma range (around 50 Hz). A broad peak in the coherence with magnitudes above 0.2 is seen up to 100–150 Hz. Above ~ 200 Hz, the coherence drops to below 0.1. The coherence across all frequencies is further reduced for increased inter-contact distances, and is negligible at 2 mm across all frequencies. The drop in coherence across frequencies with distance is similarly observed in experimental LFP data during stimulus conditions (Srinath and Ray 2014, Figure 1A). Srinath and Ray (2014) observe a peak in low-gamma LFP coherence around 40 Hz for distances up to 4 mm in two different subjects. Also an increase in coherence is seen for harmonic frequencies around 80 Hz. The baseline coherence (no visual stimulus) shows no increase in the gamma range of frequencies, except for sharp peaks due to the CRT display frequency and the second harmonic of noise (Srinath and Ray 2014). While less pronounced than in their study, also the LFP predictions show elevated coherences across greater distances than the CSD and MUA. The effect is quite visible in the color image plot (Fig. 10D), compared to the corresponding CSD and MUA (panels E and F). The effect is reminiscent of the apparent band-pass filter effect reported by Dubey and Ray (2016), in that the coherence across sites is increased and decays more slowly with distance in the gamma range compared to higher and lower frequencies. In our study, the effect occurs in the absence of temporally varying external input to the network model and is explained by network interactions. In a previous model iteration (Senk et al. 2018), we report much stronger LFP coherence in the gamma band across space, attributed to the fact that the network generated relatively strong gamma oscillations, translates into a greater band-pass filter effect.

Discussion

This study investigates a multi-layer point-neuron network model covering $4 \times 4 \text{ mm}^2$ of cortical surface at realistic neuron and connection density, amounting to ~ 3.2 million neurons and ~ 7.7 billion synapses. The model covers the same area as the 10×10 Utah multi-electrode array and accounts for spiking

activity across excitatory and inhibitory neurons in layers 2/3, 4, 5, and 6, and LFP, current source densities (CSD), and MUA in layer 2/3. Our model extends a 1 mm^2 cortical microcircuit model of macaque V1 (Potjans and Diesmann 2014; Schmidt et al. 2018a), introducing distance-dependent connection probabilities and delays. The biophysics-based LFP predictions rely on a scheme (Hagen et al. 2016) generalized to spatially structured networks.

The upscaled model reproduces asynchronous-irregular spiking activity, heterogeneous firing rates, spike-train variability consistent with observations in sensory cortex, and weak pairwise spike-train correlations. The model further exhibits spatially spreading activity with plausible propagation speed evoked by a thalamic pulse, as resulting from a brief stimulus to a part of the visual field. Finally, the model accounts for spatially correlated and coherent LFPs during spontaneous network activity, and thereby reconciles weakly correlated spiking activity with significantly correlated LFPs across space. This results from temporal filtering properties of synaptic current, filtering by neuronal cables, volume conduction, and the LFP “boosting” effect by summing over all pairwise cross-correlations between the contributing single cells, see Hagen et al. (2016, p. 4484) for details. LFP coherences are distance-dependent with a slower spatial decay around the 50 Hz low-gamma frequency compared to other frequencies, resulting in an apparent band-pass filter effect.

To our knowledge, this study is the first to address both spiking activity and LFP in a layered network model covering several square millimeters of cortical surface at full neuron and synapse density. Compared to natural cortical neuron densities of $\mathcal{O}(10^5)$ neurons/ mm^2 (see e.g. Herculano-Houzel 2009; Ribeiro et al. 2013), other studies of 2D networks often consider only one layer of excitatory and inhibitory neurons (Mehring et al. 2003; Yger et al. 2011; Voges and Perrinet 2012; Keane and Gong 2015; Schnepel et al. 2015) or two layers (Rosenbaum et al. 2017; Antólik et al. 2024), examine a smaller surface area (e.g. only 1 mm^2 , see Yger et al. 2011; Rosenbaum and Doiron 2014; Pyle and Rosenbaum 2017), and use reduced densities (e.g. about 50,000 neurons on $5 \times 5 \text{ mm}^2$, Voges and Perrinet 2012). Tomsett et al. (2014) also incorporate LFP predictions from a network of $\mathcal{O}(10^5)$ multicompartment neurons, but consider only a thin cortical slice across layers similar to *in vitro* experiments. There are also related works aiming at highly detailed anatomical models of cortical circuitry incorporating extracellular signal predictions (e.g. Billeh et al. 2020; Rimehaug et al. 2023; Reimann et al. 2024). Network downscaling without compromising first- and second order spike-train statistics requires adjusting connection strengths and background input to the decreased numbers of synapses (Albada et al. 2015), but upscaling is different: Our procedure of increasing the size of a microcircuit modifies in-degrees and background input, but preserves local recurrence and local activity statistics. Hence, the upscaled model presented here simultaneously explains the findings obtained in less complex models.

The modeled LFP amplitudes agree with spontaneous LFP amplitudes in the range $0.1 - 1 \text{ mV}$ observed experimentally (e.g. Maier et al. 2010; Hagen et al. 2015; Reyes-Puerta et al. 2016). The LFP spectra reveal an oscillation around 50 Hz, but otherwise decrease in power with frequency, akin to the power law scaling behavior in experiments. Visual cortex exhibits elevated LFP gamma power in the 30 – 80 Hz range especially during stimuli (Berens et al. 2008; Katzner et al. 2009; Jia et al. 2011; Ray and Maunsell 2011a; Xing et al. 2012; Jia et al. 2013b; Hadjipapas et al. 2015; Veit et al. 2017; Ray 2022), leading to the hypothesis that gamma oscillations have a functional role for computation

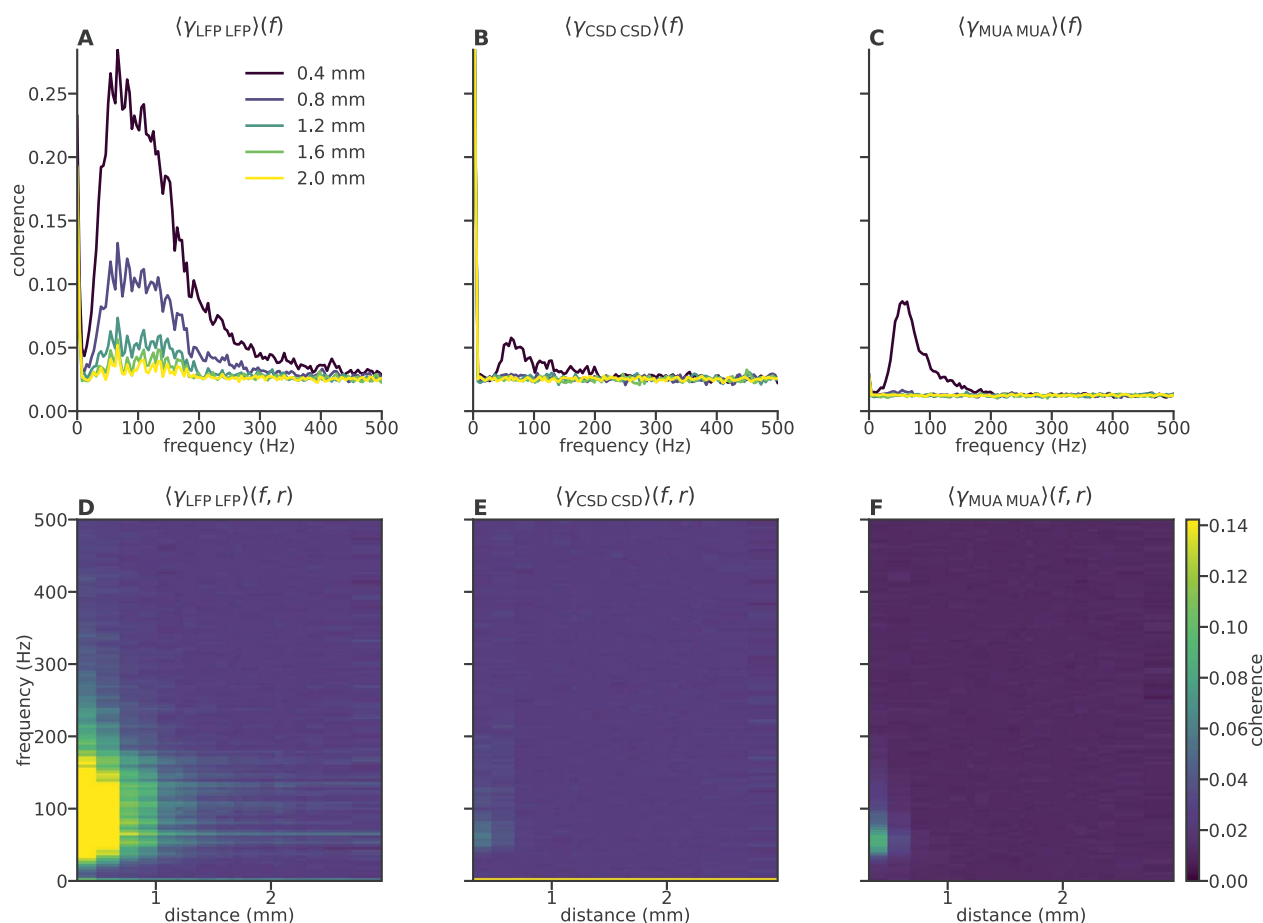


Fig. 10. Distance dependence of LFP, CSD, and MUA coherences in L2/3. **A** Pairwise LFP coherences as function of frequency for different spatial separations (color-coded) between electrode contacts, averaged over pairs with identical distance. **B** Similar to panel A but computed using the CSD signal at each electrode. **C** Similar to panels A and B but computed using the MUA signal at each electrode. **D–F** Coherence (color bar) of LFP, CSD, and MUA respectively as a function of frequency (vertical) and distance between contacts (horizontal). The upper color range is truncated at 50 of the max coherence above 10 Hz.

(Ray and Maunsell 2010; Buzsáki and Wang 2012; Jia et al. 2013a). The oscillations here result from the interplay between the excitatory and inhibitory network populations (Bos et al. 2016). The network receives an external drive with a stationary rate, does not intrinsically generate slow rate fluctuations, and is subject to active decorrelation (Tetzlaff et al. 2012). Nevertheless, the model produces correlated LFPs with a distance dependence compatible with experimental observations (Nauhaus et al. 2009). The model also reproduces elevated coherences in the low-gamma band compared to other frequencies, as also seen during visual stimulation (Jia et al. 2011; Srinath and Ray 2014). The slower spatial decay around 50 Hz in the model is consistent with a reported increased spatial LFP ‘reach’ analogous to spatial band-pass filtering in the low-gamma band (Dubey and Ray 2016). Our model shows that this effect is related to network oscillations.

The upscaled model uses exponentially decaying connection probabilities, but future work may incorporate long-range connections. Pyramidal neurons can have long horizontal axons spanning several millimeters in addition to local axonal branching. In cat and monkey visual cortex, these connections are typically patchy and connect neurons with similar orientation selectivity (Livingstone and Hubel 1984; Gilbert and Wiesel 1989; Bosking et al. 1997; Sincich and Blasdel 2001; Tanigawa et al. 2005; Buzás et al. 2006; Binzegger et al. 2007). On a similar note, the homogeneous distribution of neurons in the model is

a simplification that could be addressed in the future (Roe 2019). Inhibitory interneurons can also exhibit long-range connections (McDonald and Burkhalter 1993). Voges and Perrinet (2012) demonstrate that the fraction of local versus remote connections is crucial for the resulting network dynamics.

There are only a few comprehensive datasets detailing (distance-dependent) connection probabilities (e.g. Binzegger et al. 2004; Reimann et al. 2017). Most connectivity studies focus on specific projections, and due to different experimental protocols (Albada et al. 2022), the data are difficult to integrate. Neuron morphology appears to provide a valid first approximation for the distance dependence of projections (Amirikian 2005; Brown and Hestrin 2009; Hill et al. 2012), but the overlap between dendrites and axons alone does not explain connectivity patterns, due to target neuron-type specificity (Potjans and Diesmann 2014), specificity at the level of individual neurons (Kasthuri et al. 2015), and preferential locations of dendritic spines and synaptic boutons (Ohana et al. 2012). Algorithmic approaches pursued within large-scale consortia (e.g. Kandel et al. 2013; Markram et al. 2015; Reimann et al. 2015; Bae et al. 2023; Ding et al. 2023) will hopefully provide more accurate connectomes of different brain regions.

Activity in laminar networks depends on the boundary conditions. Here we use periodic boundary conditions, which is a common choice for 2D models with isotropic connectivity mimicking

a patch of the intact brain (e.g. Yger et al. 2011; Voges and Perrinet 2012; Rosenbaum and Doiron 2014). However, propagating activity may travel across the boundary and directly influence its own propagation, resulting in wave-front annihilation (Muller et al. 2018). An option to suppress such effects would be to sample the activity of neurons across an inner domain of a larger network (cf. Figs. 3 and 4). Larger models could also address the effects of borders to adjacent cortical areas, as anatomical borders between areas affect wave propagation (Xu et al. 2007; Muller et al. 2014). Further comparisons between waves in experimental and simulated data may follow the example of Capone et al. (2023) using a data-driven model of a whole mouse hemisphere.

Spontaneous activity in our models is driven by uncorrelated external inputs implicitly representing connections from other cortices, subcortical structures, and sensory inputs. However, mutual interactions between recurrently connected areas are expected to affect input statistics in terms of rates, spectra, and correlations (Schuecker et al. 2017; Schmidt et al. 2018a). More detailed models (e.g. Martínez-Cañada et al. 2018) representing naturalistic visual input to cortex are emerging. A recent model reconstruction of mouse visual cortex showcases the importance of thalamocortical and cortico-cortical input and feedback to the local circuit for evoked LFP and CSD signals (Billeh et al. 2020; Rimehaug et al. 2023). Inclusion of these feedback loops may bring model results closer to experimental data (e.g. Chen et al. 2022).

For signal predictions, the tool LFPy (<https://lfpypy.readthedocs.io>; Hagen et al. 2018) facilitates the calculation of current dipole moments and associated electroencephalographic (EEG) signals and magnetoencephalographic (MEG) signals (Hämäläinen et al. 1993; Nunez and Srinivasan 2006; Hagen et al. 2018). Forward-model predictions of macroscopic signals like EEG and MEG may thus provide an avenue toward a mechanistic understanding of visually evoked potentials (Sokol 1976; Neymotin et al. 2020).

Simulations of networks with $\mathcal{O}(10^6)$ neurons can be performed routinely on high-performance computing facilities (Jordan et al. 2018). However, extracellular signal predictions via the computationally demanding hybrid scheme, which relies on morphologically detailed neurons, required 3,407 core-h to initialize and 1,680 core-h/s for predicting activity, versus 180 core-h and 2.3 core-h/s, respectively, for the spiking network. Future work should adapt the kernel-based scheme of Hagen et al. (2022) for LFP, EEG, and MEG predictions from spatially organized networks.

This work represents a stepping stone for interpreting experimental data obtained by multi-electrode arrays. Simulated single-neuron and population activities can be directly compared with corresponding data in a fully digitized “integrative loop”, while the model’s simplicity makes mathematical analysis in terms of mean-field and neural field theory viable (Bos et al. 2016; Senk et al. 2020). Our hope is that the model facilitates a principled understanding of the dependence of spike correlations on distance, spatially coherent and correlated LFPs, spike-LFP relationships, and emergent spatiotemporal patterns such as waves. We therefore envision the model as a platform for future work adding further constraints iteratively and incrementally to deliver accurate predictions of brain activity.

Acknowledgements

The use of the supercomputer JURECA in Jülich was made possible by the JARA-HPC Vergabegremium and provided on the JARA-HPC Partition (VSR computation time grant JINB33). We would

like to thank Hans E. Plesser for helpful suggestions for the implementation of spatially structured networks in NEST, and Gaute T. Einevoll for providing useful feedback on the manuscript.

Funding

This project received funding from the European Union Seventh Framework Programme ([FP7/2007-2013]) under grant agreement No. 604102 (Human Brain Project, HBP), the European Union’s Horizon 2020 Framework Programme for Research and Innovation under Specific Grant Agreement No. 720270 (Human Brain Project SGA1), No. 785907 (Human Brain Project SGA2), No. 945539 (Human Brain Project SGA3), and No. 101147319 (EBRAINS 2.0 Project); the Research Council of Norway (NFR) through the grant/award number 250128 (COBRA); PreciMent Nordforsk (#164218); the Helmholtz Association through the Helmholtz Portfolio Theme “Supercomputing and Modeling for the Human Brain” and the Joint Lab “Supercomputing and Modeling for the Human Brain”; and the German Research Foundation (DFG) Priority Program “Computational Connectomics” (SPP 2041; Project 347572269). Open access publication funded by the Deutsche Forschungsgemeinschaft (DFG, German Research Foundation)—491111487.

Author contributions

Johanna Senk (Conceptualization, Data curation, Formal analysis, Investigation, Methodology, Project administration, Software, Validation, Visualization, Writing—original draft, Writing—review & editing); Espen Hagen (Conceptualization, Data curation, Formal analysis, Investigation, Methodology, Software, Supervision, Validation, Visualization, Writing—original draft, Writing—review & editing); Sacha J. van Albada (Conceptualization, Funding acquisition, Methodology, Supervision, Writing—review & editing); Markus Diesmann (Conceptualization, Funding acquisition, Methodology, Resources, Supervision, Writing—review & editing).

References

- Abeles M. *Corticonics: neural circuits of the cerebral cortex*. (1st ed.). Cambridge: Cambridge University Press; 1991. <https://doi.org/10.1017/CBO9780511574566>.
- Amirikian B. A phenomenological theory of spatially structured local synaptic connectivity. *PLoS Comput Biol*. 2005; 1:e11. <https://doi.org/10.1371/journal.pcbi.0010011>.
- Andersen P, Silfvenius H, Sundberg SH, Sveen O, Wigström H. Functional characteristics of unmyelinated fibres in the hippocampal cortex. *Brain Res*. 1978; 144:11–18. [https://doi.org/10.1016/0006-8993\(78\)90431-6](https://doi.org/10.1016/0006-8993(78)90431-6).
- Antólik J, Cagnol R, Rózsa T, Monier C, Frégnac Y, Davison AP. A comprehensive data-driven model of cat primary visual cortex. *PLoS Comput Biol*. 2024; 20:e1012342. <https://doi.org/10.1371/journal.pcbi.1012342>.
- Ascoli GA, Donohue DE, Halavi M. *NeuroMorpho.org*: a central resource for neuronal morphologies. *J Neurosci*. 2007; 27:9247–9251. <https://doi.org/10.1523/JNEUROSCI.2055-07.2007>.
- Avermann M, Tömm C, Mateo C, Gerstner W, Petersen C. Microcircuits of excitatory and inhibitory neurons in layer 2/3 of mouse barrel cortex. *J Neurophysiol*. 2012; 107:3116–3134. <https://doi.org/10.1152/jn.00917.2011>.
- Bedenbaugh P, Gerstein GL. Multiunit normalized cross correlation differs from the average single-unit normalized correlation.

- Neural Comput.* 1997; 9:1265–1275. <https://doi.org/10.1162/neco.1997.9.6.1265>.
- Benucci A, Frazor RA, Carandini M. Standing waves and traveling waves distinguish two circuits in visual cortex. *Neuron*. 2007; 55: 103–117. <https://doi.org/10.1016/j.neuron.2007.06.017>.
- Berens P, Keliris GA, Ecker AS, Logothetis NK, Tolias AS. Comparing the feature selectivity of the gamma-band of the local field potential and the underlying spiking activity in primate visual cortex. *Front Syst Neurosci.* 2008; 2:1–9. <https://doi.org/10.3389/neuro.06.002.2008>.
- Berg-Johnsen J, Langmoen IA. Temperature sensitivity of thin unmyelinated fibers in rat hippocampal cortex. *Brain Res.* 1992; 576:319–321. [https://doi.org/10.1016/0006-8993\(92\)90696-7](https://doi.org/10.1016/0006-8993(92)90696-7).
- Billeh YN, Cai B, Gratiy SL, Dai K, Iyer R, Gouwens NW, Abbasi-Asl R, Jia X, Siegle JH, Olsen SR, et al. Systematic integration of structural and functional data into multi-scale models of mouse primary visual cortex. *Neuron*. 2020; 106:388–403.e18. <https://doi.org/10.1016/j.neuron.2020.01.040>.
- Binzegger T, Douglas RJ, Martin KAC. A quantitative map of the circuit of cat primary visual cortex. *J Neurosci.* 2004; 39:8441–8453. <https://doi.org/10.1523/JNEUROSCI.1400-04.2004>.
- Binzegger T, Douglas RJ, Martin KAC. Stereotypical Bouton clustering of individual neurons in cat primary visual cortex. *J Neurosci.* 2007; 27:12242–12254. <https://doi.org/10.1523/JNEUROSCI.3753-07.2007>.
- Börgers C, Kopell N. Synchronization in networks of excitatory and inhibitory neurons with sparse, random connectivity. *Neural Comput.* 2003; 15:509–538. <https://doi.org/10.1162/089976603321192059>.
- Börgers C, Kopell N. Effects of noisy drive on rhythms in networks of excitatory and inhibitory neurons. *Neural Comput.* 2005; 17: 557–608. <https://doi.org/10.1162/0899766053019908>.
- Bos H, Diesmann M, Helias M. Identifying anatomical origins of coexisting oscillations in the cortical microcircuit. *PLoS Comput Biol.* 2016; 12:e1005132. <https://doi.org/10.1371/journal.pcbi.1005132>.
- Bosking WH, Zhang Y, Schofield B, Fitzpatrick D. Orientation selectivity and the arrangement of horizontal connections in tree shrew striate cortex. *J Neurosci.* 1997; 17:2112–2127. <https://doi.org/10.1523/JNEUROSCI.17-06-02112.1997>.
- Boucsein C, Nawrot M, Schnepel P, Aertsen A. Beyond the cortical column: abundance and physiology of horizontal connections imply a strong role for inputs from the surround. *Front Neurosci.* 2011; 5:32. <https://doi.org/10.3389/fnins.2011.00031>.
- Bringuier V, Chavane F, Glaeser L, Frégnac Y. Horizontal propagation of visual activity in the synaptic integration field of area 17 neurons. *Science*. 1999; 283:695–699. <https://doi.org/10.1126/science.283.5402.695>.
- Brown SP, Hestrin S. Intracortical circuits of pyramidal neurons reflect their long-range axonal targets. *Nature*. 2009; 457: 1133–1136. <https://doi.org/10.1038/nature07658>.
- Brunel N. Dynamics of sparsely connected networks of excitatory and inhibitory spiking neurons. *J Comput Neurosci.* 2000; 8:183–208. <https://doi.org/10.1023/A:1008925309027>.
- Brunel N, Hakim V. Fast global oscillations in networks of integrate-and-fire neurons with low firing rates. *Neural Comput.* 1999; 11: 1621–1671. <https://doi.org/10.1162/089976699300016179>.
- Budd JM, Kisvárdy ZF. Local lateral connectivity of inhibitory clutch cells in layer 4 of cat visual cortex (area 17). *Exp Brain Res.* 2001; 140:245–250. <https://doi.org/10.1007/s002210100817>.
- Buzás P, Kovács K, Ferecskó AS, Budd JML, Eysel UT, Kisvárdy ZF. Model-based analysis of excitatory lateral connections in the visual cortex. *J Comp Neurol.* 2006; 499:861–881. <https://doi.org/10.1002/cne.21134>.
- Buzsáki G, Anastassiou CA, Koch C. The origin of extracellular fields and currents – EEG, ECoG, LFP and spikes. *Nat Rev Neurosci.* 2012; 13:407–420. <https://doi.org/10.1038/nrn3241>.
- Buzsáki G, Mizuseki K. The log-dynamic brain: how skewed distributions affect network operations. *Nat Rev Neurosci.* 2014; 15: 264–278. <https://doi.org/10.1038/nrn3687>.
- Buzsáki G, Wang XJ. Mechanisms of gamma oscillations. *Annu Rev Neurosci.* 2012; 35:203–225. <https://doi.org/10.1146/annurev-neuro-062111-150444>.
- Cain N, Iyer R, Koch C, Mihalas S. The computational properties of a simplified cortical column model. *PLoS Comput Biol.* 2016; 12:e1005045. <https://doi.org/10.1371/journal.pcbi.1005045>.
- Camuñas Mesa LA, Quiroga RQ. A detailed and fast model of extracellular recordings. *Neural Comput.* 2013; 25:1191–1212. https://doi.org/10.1162/NECO_a_00433.
- Capone C, Luca CD, Bonis GD, Gutzen R, Bernava I, Pastorelli E, Simula F, Lupo C, Tonielli L, Resta F, et al. Simulations approaching data: cortical slow waves in inferred models of the whole hemisphere of mouse. *Commun Biol.* 2023; 6:266. <https://doi.org/10.1038/s42003-023-04580-0>.
- Carnevale NT, Hines ML. *The NEURON book*. Cambridge: Cambridge University Press; 2006. <https://doi.org/10.1017/CBO9780511541612>.
- Chen X, Morales-Gregorio A, Sprenger J, Kleinjohann A, Sridhar S, van Albada SJ, Grün S, Roelfsema PR. 1024-channel electrophysiological recordings in macaque V1 and V4 during resting state. *Sci Data.* 2022; 9:77. <https://doi.org/10.1038/s41597-022-01180-1>.
- Chow CC, White JA, Ritt J, Kopell N. Frequency control in synchronized networks of inhibitory neurons. *J Comput Neurosci.* 1998; 5: 407–420. <https://doi.org/10.1023/A:1008889328787>.
- Contreras D, Destexhe A, Steriade M. Intracellular and computational characterization of the intracortical inhibitory control of synchronized thalamic inputs in vivo. *J Neurophysiol.* 1997; 78: 335–350. <https://doi.org/10.1152/jn.1997.78.1.335>.
- Dahmen D, Layer M, Deutz L, Dąbrowska PA, Voges N, von Papen M, Brochier T, Riehle A, Diesmann M, Grün S, et al. Global organization of neuronal activity only requires unstructured local connectivity. *elife*. 2022; 11:e68422. <https://doi.org/10.7554/eLife.68422>.
- Dasbach S, Tetzlaff T, Diesmann M, Senk J. Dynamical characteristics of recurrent neuronal networks are robust against low synaptic weight resolution. *Front Neurosci.* 2021; 15:757790. <https://doi.org/10.3389/fnins.2021.757790>.
- De Schutter E, Van Geit W. Modeling complex neurons. In: De Schutter E., editor, *Computational Modeling methods for neuroscientists*. (1st ed.). Cambridge, MA: MIT Press; 2009, Chapter 11, pp. 260–283. <https://doi.org/10.7551/mitpress/7543.003.0013>.
- Denker M, Zehl L, Kilavik BE, Diesmann M, Brochier T, Riehle A, Grün S. LFP beta amplitude is linked to mesoscopic spatio-temporal phase patterns. *Sci Rep.* 2018; 8:1–21. <https://doi.org/10.1038/s41598-018-22990-7>.
- Destexhe A, Contreras D, Steriade M. Spatiotemporal analysis of local field potentials and unit discharges in cat cerebral cortex during natural wake and sleep states. *J Neurosci.* 1999; 19: 4595–4608. <https://doi.org/10.1523/JNEUROSCI.19-11-04595.1999>.
- Ding Z, Fahey PG, Papadopoulos S, Wang EY, Celi B, Papadopoulos C, Kunin AB, Chang A, Fu J, Ding Z, et al. Functional connectomics reveals general wiring rule in mouse visual cortex. *bioRxiv*. 2023. <https://doi.org/10.1101/2023.03.13.531369>.
- Douglas RJ, Martin KAC, Whitteridge D. A canonical microcircuit for neocortex. *Neural Comput.* 1989; 1:480–488. <https://doi.org/10.1162/neco.1989.1.4.480>.
- Dubey A, Ray S. Spatial spread of local field potential is band-pass in the primary visual cortex. *J Neurophysiol.* 2016; 116:1986–1999. <https://doi.org/10.1152/jn.00443.2016>.

- Ecker AS, Berens P, Keliris GA, Bethge M, Logothetis NK, Tolias AS. Decorrelated neuronal firing in cortical microcircuits. *Science*. 2010; 327:584–587. <https://doi.org/10.1126/science.1179867>.
- Einevoll GT, Franke F, Hagen E, Pouzat C, Harris KD. Towards reliable spike-train recordings from thousands of neurons with multielectrodes. *Curr Opin Neurobiol*. 2012; 22:11–17. <https://doi.org/10.1016/j.conb.2011.10.001>.
- Einevoll GT, Kayser C, Logothetis NK, Panzeri S. Modelling and analysis of local field potentials for studying the function of cortical circuits. *Nat Rev Neurosci*. 2013;14:770–785. <https://doi.org/10.1038/nrn3599>.
- Einevoll GT, Pettersen KH, Devor A, Ulbert I, Halgren E, Dale AM. Laminar population analysis: estimating firing rates and evoked synaptic activity from multielectrode recordings in rat barrel cortex. *J Neurophysiol*. 2007; 97:2174–2190. <https://doi.org/10.1152/jn.00845.2006>.
- Gewaltig MO, Diesmann M. NEST (NEural simulation tool). *Scholarpedia* J. 2007; 2:1430. <https://doi.org/10.4249/scholarpedia.1430>.
- Gilbert CD, Wiesel TN. Columnar specificity of intrinsic horizontal and corticocortical connections in cat visual cortex. *J Neurosci*. 1989; 9:2432–2442. <https://doi.org/10.1523/JNEUROSCI.09-07-02432.1989>.
- Graber S, Mitchell J, Kurth AC, Terhorst D, Skaar JEW, Schöfmann CM, Kunkel S, Trensche G, Haug N, Mallett D, et al. NEST 3.8. *Zenodo*. 2024. <https://doi.org/10.5281/zenodo.12624783>.
- Grinvald A, Lieke EE, Frostig RD, Hildesheim R. Cortical point-spread function and long-range lateral interactions revealed by real-time optical imaging of macaque monkey primary visual cortex. *J Neurosci*. 1994; 14:2545–2568. <https://doi.org/10.1523/JNEUROSCI.14-05-02545.1994>.
- Hadjipapas A, Lowet E, Roberts M, Peter A, Weerd PD. Parametric variation of gamma frequency and power with luminance contrast: a comparative study of human MEG and monkey LFP and spike responses. *NeuroImage*. 2015; 112:327–340. <https://doi.org/10.1016/j.neuroimage.2015.02.062>.
- Hagen E, Dahmen D, Stavrinou ML, Lindén H, Tetzlaff T, van Albada SJ, Grün S, Diesmann M, Einevoll GT. Hybrid scheme for modeling local field potentials from point-neuron networks. *Cereb Cortex*. 2016; 26:4461–4496. <https://doi.org/10.1093/cercor/bhw237>.
- Hagen E, Magnusson SH, Ness TV, Haldnes G, Babu PN, Linssen C, Morrison A, Einevoll GT. Brain signal predictions from multi-scale networks using a linearized framework. *PLoS Comput Biol*. 2022; 18:e1010353. <https://doi.org/10.1371/journal.pcbi.1010353>.
- Hagen E, Næss S, Ness TV, Einevoll GT. Multimodal modeling of neural network activity: computing LFP, ECoG, EEG, and MEG signals with LFPy 2.0. *Front Neuroinform*. 2018; 12:12. <https://doi.org/10.3389/fninf.2018.00092>.
- Hagen E, Ness TV, Khosrowshahi A, Sørensen C, Fyhn M, Hafting T, Franke F, Einevoll GT. ViSAPy: a python tool for biophysics-based generation of virtual spiking activity for evaluation of spike-sorting algorithms. *J Neurosci Methods*. 2015; 245:182–204. <https://doi.org/10.1016/j.jneumeth.2015.01.029>.
- Haldnes G, Ness TV, Næss S, Hagen E, Pettersen KH, Einevoll GT. *Electric Brain Signals: Foundations and Applications of Biophysical Modeling*. Cambridge: Cambridge University Press; 2024. <https://doi.org/10.1017/9781009039826>.
- Hämäläinen M, Haari R, Ilmoniemi RJ, Knuutila J, Lounasmaa OV. Magnetoencephalography — theory, instrumentation, and application to noninvasive studies of the working human brain. *Rev Mod Phys*. 1993; 65:413–497. <https://doi.org/10.1103/RevModPhys.65.413>.
- Hao Y, Riehle A, Brochier TG. Mapping horizontal spread of activity in monkey motor cortex using single pulse microstimulation. *Front Neural Circuits*. 2016; 10:104. <https://doi.org/10.3389/fncir.2016.00104>.
- Hardingham NR, Larkman AU. The reliability of excitatory synaptic transmission in slices of rat visual cortex in vitro is temperature dependent. *J Physiol*. 1998; 507:249–256. <https://doi.org/10.1111/j.1469-7793.1998.249bu.x>.
- Harris KD, Thiele A. Cortical state and attention. *Nat Rev Neurosci*. 2011; 12:509–523. <https://doi.org/10.1038/nrn3084>.
- Helias M, Tetzlaff T, Diesmann M. The correlation structure of local cortical networks intrinsically results from recurrent dynamics. *PLoS Comput Biol*. 2014; 10:e1003428. <https://doi.org/10.1371/journal.pcbi.1003428>.
- Hellwig B. A quantitative analysis of the local connectivity between pyramidal neurons in layers 2/3 of the rat visual cortex. *Biol Cybern*. 2000; 82:111–121. <https://doi.org/10.1007/PL00007964>.
- Herculano-Houzel S. The human brain in numbers: a linearly scaled-up primate brain. *Front Hum Neurosci*. 2009; 3:31. <https://doi.org/10.3389/neuro.09.031.2009>.
- Hill SL, Wang Y, Riachi I, Schürmann F, Markram H. Statistical connectivity provides a sufficient foundation for specific functional connectivity in neocortical neural microcircuits. *Proc Natl Acad Sci USA*. 2012; 109:E2885–E2894. <https://doi.org/10.1073/pnas.1202128109>.
- Hines ML, Davison AP, Muller E. NEURON and Python. *Front Neuroinform*. 2009; 3:1. <https://doi.org/10.3389/neuro.11.001.2009>.
- Hirsch JA, Gilbert CD. Synaptic physiology of horizontal connections in the cat's visual cortex. *J Neurosci*. 1991; 11:1800–1809. <https://doi.org/10.1523/JNEUROSCI.11-06-01800.1991>.
- Holt GR, Koch C. Electrical interactions via the extracellular potential near cell bodies. *J Comput Neurosci*. 1999; 6:169–184. <https://doi.org/10.1023/A:1008832702585>.
- Izhikevich EM, Edelman GM. Large-scale model of mammalian thalamocortical systems. *Proc Natl Acad Sci USA*. 2008; 105:3593–3598. <https://doi.org/10.1073/pnas.0712231105>.
- Jia X, Smith MA, Kohn A. Stimulus selectivity and spatial coherence of gamma components of the local field potential. *J Neurosci*. 2011; 31:9390–9403. <https://doi.org/10.1523/JNEUROSCI.0645-11.2011>.
- Jia X, Tanabe S, Kohn A. Gamma and the coordination of spiking activity in early visual cortex. *Neuron*. 2013a; 77:762–774. <https://doi.org/10.1016/j.neuron.2012.12.036>.
- Jia X, Xing D, Kohn A. No consistent relationship between gamma power and peak frequency in macaque primary visual cortex. *J Neurosci*. 2013b; 33:17–25. <https://doi.org/10.1523/JNEUROSCI.1687-12.2013>.
- Jiang X, Shen S, Cadwell CR, Berens P, Sinz F, Ecker AS, Patel S, Tolias AS. Principles of connectivity among morphologically defined cell types in adult neocortex. *Science*. 2015; 350:aac9462.
- Jordan J, Ippen T, Helias M, Kitayama I, Sato M, Igarashi J, Diesmann M, Kunkel S. Extremely scalable spiking neuronal network simulation code: from laptops to exascale computers. *Front Neuroinform*. 2018; 12:2. <https://doi.org/10.3389/fninf.2018.00002>.
- Kajikawa Y, Schroeder CE. How local is the local field potential? *Neuron*. 2011; 72:847–858. <https://doi.org/10.1016/j.neuron.2011.09.029>.
- Kandel ER, Markram H, Matthews PM, Yuste R, Koch C. Neuroscience thinks big (and collaboratively). *Nat Rev Neurosci*. 2013; 14:659–664. <https://doi.org/10.1038/nrn3578>.
- Kang Y, Kaneko T, Ohishi H, Endo K, Araki T. Spatiotemporally differential inhibition of pyramidal cells in the cat motor cortex. *J Neurophysiol*. 1994; 71:280–293. <https://doi.org/10.1152/jn.1994.71.1.280>.

- Kasthuri N, Hayworth KJ, Berger DR, Schalek RL, Conchello JA, Knowles-Barley S, Lee D, Vázquez-Reina A, Kaynig V, Jones TR, et al. Saturated reconstruction of a volume of neocortex. *Cell*. 2015: 162:648–661. <https://doi.org/10.1016/j.cell.2015.06.054>.
- Katz B, Miledi R. The effect of temperature on the synaptic delay at the neuromuscular junction. *J Physiol*. 1965: 181:656–670. <https://doi.org/10.1113/jphysiol.1965.sp007790>.
- Katzner S, Nauhaus I, Benucci A, Bonin V, Ringach DL, Carandini M. Local origin of field potentials in visual cortex. *Neuron*. 2009: 61: 35–41. <https://doi.org/10.1016/j.neuron.2008.11.016>.
- Kauth K, Stadtmann T, Sobhani V, Gemmeke T. Neuroaix-framework: design of future neuroscience simulation systems exhibiting execution of the cortical microcircuit model 20x faster than biological real-time. *Front Comput Neurosci*. 2023: 17:17. <https://doi.org/10.3389/fncom.2023.1144143>.
- Keane A, Gong P. Propagating waves can explain irregular neural dynamics. *J Neurosci*. 2015: 35:1591–1605. <https://doi.org/10.1523/JNEUROSCI.1669-14.2015>.
- Kisvárdy ZF, Eysel UT. Cellular organization of reciprocal patchy networks in layer III of cat visual cortex (area 17). *Neuroscience*. 1992: 46:275–286. [https://doi.org/10.1016/0306-4522\(92\)90050-C](https://doi.org/10.1016/0306-4522(92)90050-C).
- Klein C, Evrard HC, Shapcott KA, Haverkamp S, Logothetis NK, Schmid MC. Cell-targeted optogenetics and electrical microstimulation reveal the primate koniocellular projection to supragranular visual cortex. *Neuron*. 2016: 90:143–151. <https://doi.org/10.1016/j.neuron.2016.02.036>.
- Korcsak-Gorzo A, Linssen C, Albers J, Dasbach S, Duarte R, Kunkel S, Morrison A, Senk J, Stapmanns J, Tetzlaff T, et al. *Phenomenological modeling of diverse and heterogeneous synaptic dynamics at natural density*, New York, NY: Springer US, 2024. pp. 277–321. https://doi.org/10.1007/978-1-0716-4019-7_15.
- Larkum ME, Zhu JJ, Sakmann B. Dendritic mechanisms underlying the coupling of the dendritic with the axonal action potential initiation zone of adult rat layer 5 pyramidal neurons. *J Physiol*. 2001: 533:447–466. <https://doi.org/10.1111/j.1469-7793.2001.0447.a.x>.
- Łęski S, Lindén H, Tetzlaff T, Pettersen KH, Einevoll GT. Frequency dependence of signal power and spatial reach of the local field potential. *PLoS Comput Biol*. 2013: 9:e1003137. <https://doi.org/10.1371/journal.pcbi.1003137>.
- Leung LS. Nonlinear feedback model of neuronal populations in hippocampal CA1 region. *J Neurophysiol*. 1982: 47:845–868. <https://doi.org/10.1152/jn.1982.47.5.845>.
- Levy RB, Reyes AD. Spatial profile of excitatory and inhibitory synaptic connectivity in mouse primary auditory cortex. *J Neurosci*. 2012: 32:5609–5619. <https://doi.org/10.1523/JNEUROSCI.5158-11.2012>.
- Lindén H, Hagen E, Łęski S, Norheim ES, Pettersen KH, Einevoll GT. LFPy: a tool for biophysical simulation of extracellular potentials generated by detailed model neurons. *Front Neuroinform*. 2014: 7:41. <https://doi.org/10.3389/fninf.2013.00041>.
- Lindén H, Pettersen KH, Einevoll GT. Intrinsic dendritic filtering gives low-pass power spectra of local field potentials. *J Comput Neurosci*. 2010: 29:423–444. <https://doi.org/10.1007/s10827-010-0245-4>.
- Lindén H, Tetzlaff T, Potjans TC, Pettersen KH, Grün S, Diesmann M, Einevoll GT. Modeling the spatial reach of the LFP. *Neuron*. 2011: 72:859–872. <https://doi.org/10.1016/j.neuron.2011.11.006>.
- Livingstone MS, Hubel DH. Specificity of intrinsic connections in primate primary visual cortex. *J Neurosci*. 1984: 4:2830–2835. <https://doi.org/10.1523/JNEUROSCI.04-11-02830.1984>.
- Lohmann H, Rörig B. Long-range horizontal connections between supragranular pyramidal cells in the extrastriate visual cortex of the rat. *J Comp Neurol*. 1994: 344:543–558. <https://doi.org/10.1002/cne.903440405>.
- Maier A, Adams GK, Aura C, Leopold DA. Distinct superficial and deep laminar domains of activity in the visual cortex during rest and stimulation. *Front Syst Neurosci*. 2010: 4:31. <https://doi.org/10.3389/fnsys.2010.00031>.
- Mainen ZF, Sejnowski TJ. Influence of dendritic structure on firing pattern in model neocortical neurons. *Nature*. 1996: 382:363–366. <https://doi.org/10.1038/382363a0>.
- Markram H, Muller E, Ramaswamy S, Reimann MW, Abdellah M, Sanchez CA, Ailamaki A, Alonso-Nanclares L, Antille N, Arsever S, et al. Reconstruction and simulation of neocortical microcircuitry. *Cell*. 2015: 163:456–492. <https://doi.org/10.1016/j.cell.2015.09.029>.
- Martínez-Cañada P, Mobarhan MH, Halmes G, Fyhn M, Morillas C, Pelayo F, Einevoll GT. Biophysical network modeling of the dLGN circuit: effects of cortical feedback on spatial response properties of relay cells. *PLoS Comput Biol*. 2018: 14:e1005930. <https://doi.org/10.1371/journal.pcbi.1005930>.
- Maynard EM, Nordhausen CT, Normann RA. The Utah intracortical electrode array: a recording structure for potential brain-computer interfaces. *Electroencephalogr Clin Neurophysiol*. 1997: 102:228–239. [https://doi.org/10.1016/S0013-4694\(96\)95176-0](https://doi.org/10.1016/S0013-4694(96)95176-0).
- McDonald CT, Burkhalter A. Organisation of long-range inhibitory connections within rat visual cortex. *J Neurosci*. 1993: 13:768–781. <https://doi.org/10.1523/JNEUROSCI.13-02-00768.1993>.
- Mehring C, Hehl U, Kubo M, Diesmann M, Aertsen A. Activity dynamics and propagation of synchronous spiking in locally connected random networks. *Biol Cybern*. 2003: 88:395–408. <https://doi.org/10.1007/s00422-002-0384-4>.
- MICrONS Consortium, Bae JA, Baptiste M, Bishop CA, Bodor AL, Brittain D, Buchanan J, Bumbarger DJ, Castro MA, Celii B, et al. Functional connectomics spanning multiple areas of mouse visual cortex. *bioRxiv*. 2023. <https://doi.org/10.1101/2021.07.28.454025>.
- Mitzdorf U. Current source-density method and application in cat cerebral cortex: investigation of evoked potentials and EEG phenomena. *Physiol Rev*. 1985: 65:37–100. <https://doi.org/10.1152/physrev.1985.65.1.37>.
- Mochizuki Y, Onaga T, Shimazaki H, Shimokawa T, Tsubo Y, Kimura R, Saiki A, Sakai Y, Isomura Y, Fujisawa S, et al. Similarity in neuronal firing regimes across mammalian species. *J Neurosci*. 2016: 36:5736–5747. <https://doi.org/10.1523/JNEUROSCI.0230-16.2016>.
- Muller L, Chavane F, Reynolds J, Sejnowski TJ. Cortical travelling waves: mechanisms and computational principles. *Nat Rev Neurosci*. 2018: 19:255–268. <https://doi.org/10.1038/nrn.2018.20>.
- Muller L, Reynaud A, Chavane F, Destexhe A. The stimulus-evoked population response in visual cortex of awake monkey is a propagating wave. *Nat Commun*. 2014: 5:5. <https://doi.org/10.1038/ncomms4675>.
- Murakoshi T, Guo JZ, Ichinose T. Electrophysiological identification of horizontal synaptic connections in rat visual cortex in vitro. *Neurosci Lett*. 1993: 163:211–214. [https://doi.org/10.1016/0304-3940\(93\)90385-X](https://doi.org/10.1016/0304-3940(93)90385-X).
- Nauhaus I, Busse L, Carandini M, Ringach DL. Stimulus contrast modulates functional connectivity in visual cortex. *Nat Neurosci*. 2009: 12:70–76. <https://doi.org/10.1038/nn.2232>.
- Nauhaus I, Busse L, Ringach DL, Carandini M. Robustness of traveling waves in ongoing activity of visual cortex. *J Neurosci*. 2012: 32: 3088–3094. <https://doi.org/10.1523/JNEUROSCI.5827-11.2012>.
- Nelson MJ, Pouget P. Do electrode properties create a problem in interpreting local field potential recordings? *J Neurophysiol*. 2010: 103:2315–2317. <https://doi.org/10.1152/jn.00157.2010>.

- Nelson MJ, Pouget P, Nilsen EA, Patten CD, Schall JD. Review of signal distortion through metal microelectrode recording circuits and filters. *J Neurosci Methods*. 2008; 169:141–157. <https://doi.org/10.1016/j.jneumeth.2007.12.010>.
- Ness TV, Chintaluri HC, Potworowski J, Łęski S, Głąbska H, Wójcik DK, Einevoll GT. Modelling and analysis of electrical potentials recorded in multielectrode arrays (MEAs). *Neuroinformatics*. 2015; 13:403–426. <https://doi.org/10.1007/s12021-015-9265-6>.
- Neymotin SA, Daniels DS, Caldwell B, McDougal RA, Carnevale NT, Jas M, Moore CI, Hines ML, Härmäläinen M, Jones SR. Human neocortical neurosolver (HNN), a new software tool for interpreting the cellular and network origin of human MEG/EEG data. *elife*. 2020; 9:e51214. <https://doi.org/10.7554/eLife.51214>.
- Nicholson C, Freeman JA. Theory of current source-density analysis and determination of conductivity tensor for anuran cerebellum. *J Neurophysiol*. 1975; 38:356–368. <https://doi.org/10.1152/jn.1975.38.2.356>.
- Nordlie E, Gewaltig MO, Plesser HE. Towards reproducible descriptions of neuronal network models. *PLoS Comput Biol*. 2009; 5:e1000456. <https://doi.org/10.1371/journal.pcbi.1000456>.
- Nunez PL, Srinivasan R. *Electric fields of the brain, the neurophysics of EEG*. (2nd ed.). New York: Oxford University Press, Inc.; 2006. <https://doi.org/10.1093/acprof:oso/9780195050387.001.0001>.
- Ohana O, Portner H, Martin KAC. Fast recruitment of recurrent inhibition in the cat visual cortex. *PLOS ONE*. 2012; 7:e40601. <https://doi.org/10.1371/journal.pone.0040601>.
- Packer AM, Yuste R. Dense, unspecific connectivity of neocortical parvalbumin-positive interneurons: a canonical microcircuit for inhibition? *J Neurosci*. 2011; 31:13260–13271. <https://doi.org/10.1523/JNEUROSCI.3131-11.2011>.
- Perin R, Berger TK, Markram H. A synaptic organizing principle for cortical neuronal groups. *Proc Natl Acad Sci USA*. 2011; 108:5419–5424. <https://doi.org/10.1073/pnas.1016051108>.
- Perkel DH, Gerstein GL, Moore GP. Neuronal spike trains and stochastic point processes. I. The single spike train. *Biomed Pharmacol J*. 1967; 7:391–418. [https://doi.org/10.1016/S0006-3495\(67\)86596-2](https://doi.org/10.1016/S0006-3495(67)86596-2).
- Pettersen KH, Devor A, Ulbert I, Dale AM, Einevoll GT. Current-source density estimation based on inversion of electrostatic forward solution: effects of finite extent of neuronal activity and conductivity discontinuities. *J Neurosci Methods*. 2006; 154:116–133. <https://doi.org/10.1016/j.jneumeth.2005.12.005>.
- Pettersen KH, Hagen E, Einevoll GT. Estimation of population firing rates and current source densities from laminar electrode recordings. *J Comput Neurosci*. 2008; 24:291–313. <https://doi.org/10.1007/s10827-007-0056-4>.
- Potjans TC, Diesmann M. The cell-type specific cortical microcircuit: relating structure and activity in a full-scale spiking network model. *Cereb Cortex*. 2014; 24:785–806. <https://doi.org/10.1093/cercor/bhs358>.
- Potworowski J, Jakuczun W, Łęski S, Wójcik D. Kernel current source density method. *Neural Comput*. 2012; 24:541–575. https://doi.org/10.1162/NECO_a_00236.
- Prakash SS, Das A, Kanth ST, Mayo JP, Ray S. Decoding of attentional state using high-frequency local field potential is as accurate as using spikes. *Cereb Cortex*. 2021; 31:4314–4328. <https://doi.org/10.1093/cercor/bhab088>.
- Pyle R, Rosenbaum R. Spatiotemporal dynamics and reliable computations in recurrent spiking neural networks. *Phys Rev Lett*. 2017; 118:018103. <https://doi.org/10.1103/PhysRevLett.118.018103>.
- Quiroga RQ. Spike sorting. *Scholarpedia J*. 2007; 2:3583. <https://doi.org/10.4249/scholarpedia.3583>.
- Ramaswamy S, Courcol JD, Abdellah M, Adaszewski SR, Antille N, Arsever S, Atnekeng G, Bilgili A, Brukau Y, Chalimourda A, et al. The neocortical microcircuit collaboration portal: a resource for rat somatosensory cortex. *Front Neural Circuits*. 2015; 9:44. <https://doi.org/10.3389/fncir.2015.00044>.
- Ray S. Spike—gamma phase relationship in the visual cortex. *Annual Review of Vision Science*. 2022; 8:361–381. <https://doi.org/10.1146/annurev-vision-100419-104530>.
- Ray S, Maunsell JHR. Differences in gamma frequencies across visual cortex restrict their possible use in computation. *Neuron*. 2010; 67:885–896. <https://doi.org/10.1016/j.neuron.2010.08.004>.
- Ray S, Maunsell JHR. Different origins of gamma rhythm and high-gamma activity in macaque visual cortex. *PLoS Comput Biol*. 2011a; 9:e1000610. <https://doi.org/10.1371/journal.pbio.1000610>.
- Ray S, Maunsell JHR. Network rhythms influence the relationship between spike-triggered local field potential and functional connectivity. *J Neurosci*. 2011b; 31:12674–12682. <https://doi.org/10.1523/JNEUROSCI.1856-11.2011>.
- Reimann MW, Bolanös-Puchet S, Courcol JD, Egas Santander D, Arnaudon A, Coste B, Delalandre F, Delemontex T, Devresse A, Dictus H, et al. Modeling and simulation of neocortical micro- and mesocircuitry. Part I: Modeling Anatomy. *bioRxiv*. 2024. <https://doi.org/10.1101/2022.08.11.503144>.
- Reimann MW, Horlemann AL, Ramaswamy S, Muller EB, Markram H. Morphological diversity strongly constrains synaptic connectivity and plasticity. *Cereb Cortex*. 2017; 27:4570–4585. <https://doi.org/10.1093/cercor/bhx150>.
- Reimann MW, King JG, Muller EB, Ramaswamy S, Markram H. An algorithm to predict the connectome of neural microcircuits. *Front Comput Neurosci*. 2015; 9:120. <https://doi.org/10.3389/fncom.2015.00120>.
- Renart A, De La Rocha J, Bartho P, Hollender L, Parga N, Reyes A, Harris KD. The asynchronous state in cortical circuits. *Science*. 2010; 327:587–590. <https://doi.org/10.1126/science.1179850>.
- Reyes-Puerta V, Yang JW, Siwek ME, Kilb W, Sun JJ, Luhmann HJ. Propagation of spontaneous slow-wave activity across columns and layers of the adult rat barrel cortex in vivo. *Brain Struct Funct*. 2016; 221:4429–4449. <https://doi.org/10.1007/s00429-015-1173-x>.
- Ribeiro PFM, Ventura-Antunes L, Gabi M, Mota B, Grinberg LT, Farfel JM, Ferretti-Rebustini REL, Leite REP, Filho WJ, Herculano-Houzel S. The human cerebral cortex is neither one nor many: neuronal distribution reveals two quantitatively different zones in the gray matter, three in the white matter, and explains local variations in cortical folding. *Front Neuroanat*. 2013; 7:28. <https://doi.org/10.3389/fnana.2013.00028>.
- Riehle A, Wirtsohn S, Grün S, Brochier T. Mapping the spatio-temporal structure of motor cortical LFP and spiking activities during reach-to-grasp movements. *Front Neural Circuits*. 2013; 7:48. <https://doi.org/10.3389/fncir.2013.00048>.
- Rimehaug AE, Stasik AJ, Hagen E, Billeh YN, Siegle JH, Dai K, Olsen SR, Koch C, Einevoll GT, Arkhipov A. Uncovering circuit mechanisms of current sinks and sources with biophysical simulations of primary visual cortex. *elife*. 2023; 12:e87169. <https://doi.org/10.7554/eLife.87169>.
- Robinson DA. The electrical properties of metal microelectrodes. *Proc IEEE*. 1968; 56:1065–1071. <https://doi.org/10.1109/PROC.1968.6458>.
- Roe AW. Columnar connectome: toward a mathematics of brain function. *Network Neuroscience*. 2019; 3:779–791. https://doi.org/10.1162/netn_a_00088.
- Rosenbaum R, Doiron B. Balanced networks of spiking neurons with spatially dependent recurrent connections. *Phys Rev X*. 2014; 4:021039. <https://doi.org/10.1103/PhysRevX.4.021039>.

- Rosenbaum R, Smith MA, Kohn A, Rubin JE, Doiron B. The spatial structure of correlated neuronal variability. *Nat Neurosci*. 2017; 20: 107–114. <https://doi.org/10.1038/nn.4433>.
- Rosenbaum R, Trousdale J, Josic K. The effects of pooling on correlated neural variability. *Front Neurosci*. 2011; 5:58. <https://doi.org/10.3389/fnins.2011.00058>.
- Rotter S, Diesmann M. Exact digital simulation of time-invariant linear systems with applications to neuronal modeling. *Biol Cybern*. 1999; 81:381–402. <https://doi.org/10.1007/s004220050570>.
- Rubino D, Robbins KA, Hatsopoulos NG. Propagating waves mediate information transfer in the motor cortex. *Nat Neurosci*. 2006; 9: 1549–1557. <https://doi.org/10.1038/nn1802>.
- Sabatini BL, Regehr WG. Timing of neurotransmission at fast synapses in the mammalian brain. *Nature*. 1996; 384:170–172. <https://doi.org/10.1038/384170a0>.
- Salin PA, Prince DA. Electrophysiological mapping of GABAA receptor-mediated inhibition in adult rat somatosensory cortex. *J Neurophysiol*. 1996; 75:1589–1600. <https://doi.org/10.1152/jn.1996.75.4.1589>.
- Sato TK, Nauhaus I, Carandini M. Traveling waves in visual cortex. *Neuron*. 2012; 75:218–229. <https://doi.org/10.1016/j.neuron.2012.06.029>.
- Schmidt M, Bakker R, Hilgetag CC, Diesmann M, van Albada SJ. Multi-scale account of the network structure of macaque visual cortex. *Brain Struct Funct*. 2018a; 223:1409–1435. <https://doi.org/10.1007/s00429-017-1554-4>.
- Schmidt M, Bakker R, Shen K, Bezgin G, Diesmann M, van Albada SJ. A multi-scale layer-resolved spiking network model of resting-state dynamics in macaque visual cortical areas. *PLoS Comput Biol*. 2018b; 14:e1006359. <https://doi.org/10.1371/journal.pcbi.1006359>.
- Schnepel P, Kumar A, Zohar M, Aertsen A, Boucsein C. Physiology and impact of horizontal connections in rat neocortex. *Cereb Cortex*. 2015; 25:3818–3835. <https://doi.org/10.1093/cercor/bhu265>.
- Schuecker J, Schmidt M, van Albada SJ, Diesmann M, Helias M. Fundamental activity constraints lead to specific interpretations of the connectome. *PLoS Comput Biol*. 2017; 13:e1005179. <https://doi.org/10.1371/journal.pcbi.1005179>.
- Schwalger T, Deger M, Gerstner W. Towards a theory of cortical columns: from spiking neurons to interacting neural populations of finite size. *PLoS Comput Biol*. 2017; 13:e1005507. <https://doi.org/10.1371/journal.pcbi.1005507>.
- Senk J, Hagen E, van Albada SJ, Diesmann M. Reconciliation of weak pairwise spike-train correlations and highly coherent local field potentials across space. *arXiv*. 2018, 1805.10235v1 [q-bio.NC]. <https://doi.org/10.48550/arXiv.1805.10235>.
- Senk J, Korvasová K, Schuecker J, Hagen E, Tetzlaff T, Diesmann M, Helias M. Conditions for wave trains in spiking neural networks. *Phys Rev Res*. 2020; 2:023174. <https://doi.org/10.1103/PhysRevResearch.2.023174>.
- Senk J, Kriener B, Djurfeldt M, Voges N, Jiang HJ, Schüttler L, Gramelsberger G, Diesmann M, Plesser HE, van Albada SJ. Connectivity concepts in neuronal network modeling. *PLoS Comput Biol*. 2022; 18:e1010086. <https://doi.org/10.1371/journal.pcbi.1010086>.
- Sheng TK. The distance between two random points in plane regions. *Adv Appl Probab*. 1985; 17:748–773. <https://doi.org/10.2307/1427086>.
- Sherwood CC, Miller SB, Karl M, Stimpson CD, Phillips KA, Jacobs B, Hof PR, Raghanti MA, Smaers JB. Invariant synapse density and neuronal connectivity scaling in primate neocortical evolution. *Cereb Cortex*. 2020; 30:5604–5615. <https://doi.org/10.1093/cercor/bhaa149>.
- Shinomoto S, Shima K, Tanji J. Differences in spiking patterns among cortical neurons. *Neural Comput*. 2003; 15:2823–2842. <https://doi.org/10.1162/089976603322518759>.
- Sincich LC, Blasdel GG. Oriented axon projections in primary visual cortex of the monkey. *J Neurosci*. 2001; 21:4416–4426. <https://doi.org/10.1523/JNEUROSCI.21-12-04416.2001>.
- Smith MA, Kohn A. Spatial and temporal scales of neuronal correlation in primary visual cortex. *J Neurosci*. 2008; 28:12591–12603. <https://doi.org/10.1523/JNEUROSCI.2929-08.2008>.
- Softky WR, Koch C. The highly irregular firing of cortical cells is inconsistent with temporal integration of random EPSPs. *J Neurosci*. 1993; 13:334–350. <https://doi.org/10.1523/JNEUROSCI.13-01-00334.1993>.
- Sokol S. Visually evoked potentials: theory, techniques and clinical applications. *Surv Ophthalmol*. 1976; 21:18–44. [https://doi.org/10.1016/0039-6257\(76\)90046-1](https://doi.org/10.1016/0039-6257(76)90046-1).
- Srinath R, Ray S. Effect of amplitude correlations on coherence in the local field potential. *J Neurophysiol*. 2014; 112:741–751. <https://doi.org/10.1152/jn.00851.2013>.
- Stepanyants A, Hirsch JA, Martinez LM, Kisvárdy ZF, Ferecskó AS, Chklovskii DB. Local potential connectivity in cat primary visual cortex. *Cereb Cortex*. 2007; 18:13–28. <https://doi.org/10.1093/cercor/bhm027>.
- Stepanyants A, Martinez LM, Ferecskó AS, Kisvárdy ZF. The fractions of short- and long-range connections in the visual cortex. *Proc Natl Acad Sci USA*. 2009; 106:3555–3560. <https://doi.org/10.1073/pnas.0810390106>.
- Swadlow HA, Gusev AG, Bezudnaya T. Activation of a cortical column by a thalamocortical impulse. *J Neurosci*. 2002; 22:7766–7773. <https://doi.org/10.1523/JNEUROSCI.22-17-07766.2002>.
- Takahashi K, Kim S, Coleman TP, Brown KA, Suminski AJ, Best MD, Hatsopoulos NG. Large-scale spatiotemporal spike patterning consistent with wave propagation in motor cortex. *Nat Commun*. 2015; 6:1–11. <https://doi.org/10.1038/ncomms8169>.
- Tanigawa H, Wang Q, Fujita I. Organization of horizontal axons in the inferior temporal cortex and primary visual cortex of the macaque monkey. *Cereb Cortex*. 2005; 15:1887–1899. <https://doi.org/10.1093/cercor/bhi067>.
- Tetzlaff T, Helias M, Einevoll GT, Diesmann M. Decorrelation of neural-network activity by inhibitory feedback. *PLoS Comput Biol*. 2012; 8:e1002596. <https://doi.org/10.1371/journal.pcbi.1002596>.
- Thomson AM, West DC, Wang Y, Bannister AP. Synaptic connections and small circuits involving excitatory and inhibitory neurons in layer 2-5 of adult rat and cat neocortex: triple intracellular recordings and biocytin labelling in vitro. *Cereb Cortex*. 2002; 12: 936–953. <https://doi.org/10.1093/cercor/12.9.936>.
- Thörnig P. JURECA: data centric and booster modules implementing the modular supercomputing architecture at Jülich supercomputing Centre. *JLSRF*. 2021; 7:7. <https://doi.org/10.17815/jlsrf-7-182>.
- Tomsett RJ, Ainsworth M, Thiele A, Sanayei M, Chen X, Gieselmann MA, Whittington MA, Cunningham MO, Kaiser M. Virtual electrode recording tool for EXtracellular potentials (VERTX): comparing multi-electrode recordings from simulated and biological mammalian cortical tissue. *Brain Struct Funct*. 2014; 220:2333–2353. <https://doi.org/10.1007/s00429-014-0793-x>.
- Tukey JW. *Exploratory data analysis*. Reading, Mass: Pearson; 1977.
- van Albada SJ, Helias M, Diesmann M. Scalability of asynchronous networks is limited by one-to-one mapping between effective connectivity and correlations. *PLoS Comput Biol*. 2015; 11:e1004490. <https://doi.org/10.1371/journal.pcbi.1004490>.

- van Albada SJ, Morales-Gregorio A, Dickscheid T, Goulas A, Bakker R, Bludau S, Palm G, Hilgetag CC, Diesmann M. Bringing anatomical information into neuronal network models. In: Giugliano M, Negrello M, Linaro D, editors, *Computational modelling of the brain: modelling approaches to cells, circuits and networks*. Cham: Springer International Publishing; 2022, pp. 201–234. https://doi.org/10.1007/978-3-030-89439-9_9.
- van Albada SJ, Rowley AG, Senk J, Hopkins M, Schmidt M, Stokes AB, Lester DR, Diesmann M, Furber SB. Performance comparison of the digital neuromorphic hardware SpiNNaker and the neural network simulation software NEST for a full-scale cortical microcircuit model. *Front Neurosci*. 2018; 12:291. <https://doi.org/10.3389/fnins.2018.00291>.
- van Kerkoerle T, Self MW, Dagnino B, Gariel-Mathis MA, Poort J, van der Togt C, Roelfsema PR. Alpha and gamma oscillations characterize feedback and feedforward processing in monkey visual cortex. *Proc Natl Acad Sci USA*. 2014; 111:14332–14341. <https://doi.org/10.1073/pnas.1402773111>.
- Veit J, Hakim R, Jädi MP, Sejnowski TJ, Adesnik H. Cortical gamma band synchronization through somatostatin interneurons. *Nat Neurosci*. 2017; 20:951–959. <https://doi.org/10.1038/nn.4562>.
- Voges N, Perrinet L. Complex dynamics in recurrent cortical networks based on spatially realistic connectivities. *Front Comput Neurosci*. 2012; 6:41. <https://doi.org/10.3389/fncom.2012.00041>.
- Voges N, Schüz A, Aertsen A, Rotter S. A modeler's view on the spatial structure of intrinsic horizontal connectivity in the neocortex. *Prog Neurobiol*. 2010; 92:277–292. <https://doi.org/10.1016/j.pneurobio.2010.05.001>.
- Vugrin KW, Swiler LP, Roberts RM, Stucky-Mack NJ, Sullivan SP. Confidence region estimation techniques for nonlinear regression in groundwater flow: three case studies. *Water Resour Res*. 2007; 43:W03423. <https://doi.org/10.1029/2005WR004804>.
- Wagatsuma N, Potjans TC, Diesmann M, Fukai T. Layer-dependent attentional processing by top-down signals in a visual cortical microcircuit model. *Front Comput Neurosci*. 2011; 5:31. <https://doi.org/10.3389/fncom.2011.00031>.
- Wang XJ, Buzsáki G. Gamma oscillation by synaptic inhibition in a hippocampal interneuronal network model. *J Neurosci*. 1996; 16:6402–6413. <https://doi.org/10.1523/JNEUROSCI.16-20-06402.1996>.
- Welch PD. The use of fast fourier transform for the estimation of power spectra: a method based on time averaging over short, modified periodograms. *IEEE Trans Audio Electroacoust*. 1967; 15: 70–73. <https://doi.org/10.1109/TAU.1967.1161901>.
- Whittington MA, Traub RD, Jefferys JGR. Synchronized oscillations in interneuron networks driven by metabotropic glutamate receptor activation. *Nature*. 1995; 373:612–615. <https://doi.org/10.1038/373612a0>.
- Whittington MA, Traub RD, Kopell N, Ermentrout B, Buhl EH. Inhibition-based rhythms: experimental and mathematical observations on network dynamics. *Int J Psychophysiol*. 2000; 38: 315–336. [https://doi.org/10.1016/S0167-8760\(00\)00173-2](https://doi.org/10.1016/S0167-8760(00)00173-2).
- Wu JY, Huang X, Zhang C. Propagating waves of activity in the neocortex: what they are, what they do. *Neuroscientist*. 2008; 14: 487–502. <https://doi.org/10.1177/1073858408317066>.
- Xing D, Yeh CI, Burns S, Shapley RM. Laminar analysis of visually evoked activity in the primary visual cortex. *Proc Natl Acad Sci USA*. 2012; 109:13871–13876. <https://doi.org/10.1073/pnas.1201478109>.
- Xu W, Huang X, Takagaki K, young Wu J. Compression and reflection of visually evoked cortical waves. *Neuron*. 2007; 55:119–129. <https://doi.org/10.1016/j.neuron.2007.06.016>.
- Yger P, El Boustani S, Destexhe A, Frégnac Y. Topologically invariant macroscopic statistics in balanced networks of conductance-based integrate-and-fire neurons. *J Comput Neurosci*. 2011; 31: 229–245. <https://doi.org/10.1007/s10827-010-0310-z>.
- Zanos TP, Mineault PJ, Nasiotis KT, Guitton D, Pack CC. A sensorimotor role for traveling waves in primate visual cortex. *Neuron*. 2015; 85:615–627. <https://doi.org/10.1016/j.neuron.2014.12.043>.